Influence of Particle Aspect Ratio on the Midinfrared Extinction Spectra of Wavelength-Sized Ice Crystals

Robert Wagner,* Stefan Benz, Ottmar Möhler, Harald Saathoff, Martin Schnaiter, and Thomas Leisner

Institute of Meteorology and Climate Research, Forschungszentrum Karlsruhe, Karlsruhe, Germany

Received: May 30, 2007; In Final Form: September 19, 2007

We have used the T-matrix method and the discrete dipole approximation to compute the midinfrared extinction cross-sections (4500−800 cm^{-1}) of randomly oriented circular ice cylinders for aspect ratios extending up to 10 for oblate and down to $^1/_6$ for prolate particle shapes. Equal-volume sphere diameters ranged from 0.1 to 10 μm for both particle classes. A high degree of particle asphericity provokes a strong distortion of the spectral habitus compared to the extinction spectrum of compactly shaped ice crystals with an aspect ratio around 1. The magnitude and the sign (increase or diminution) of the shape-related changes in both the absorption and the scattering cross-sections crucially depend on the particle size and the values for the real and imaginary part of the complex refractive index. When increasing the particle asphericity for a given equal-volume sphere diameter, the values for the overall extinction cross-sections may change in opposite directions for different parts of the spectrum. We have applied our calculations to the analysis of recent expansion cooling experiments on the formation of cirrus clouds, performed in the large coolable aerosol and cloud chamber AIDA of Forschungszentrum Karlsruhe at a temperature of 210 K. Depending on the nature of the seed particles and the temperature and relative humidity characteristics during the expansion, ice crystals of various shapes and aspect ratios could be produced. For a particular expansion experiment, using Illite mineral dust particles coated with a layer of secondary organic matter as seed aerosol, we have clearly detected the spectral signatures characteristic of strongly aspherical ice crystal habits in the recorded infrared extinction spectra. We demonstrate that the number size distributions and total number concentrations of the ice particles that were generated in this expansion run can only be accurately derived from the recorded infrared spectra when employing aspect ratios as high as 10 in the retrieval approach. Remarkably, the measured spectra could also be accurately fitted when employing an aspect ratio of 1 in the retrieval. The so-deduced ice particle number concentrations, however, exceeded the true values, determined with an optical particle counter, by more than 1 order of magnitude. Thus, the shape-induced spectral changes between the extinction spectra of platelike ice crystals of aspect ratio 10 and compactly shaped particles of aspect ratio 1 can be efficiently balanced by deforming the true number size distribution of the ice cloud. As a result of this severe size/shape ambiguity in the spectral analysis, we consider it indispensable to cross-check the infrared retrieval results of wavelength-sized ice particles with independent reference measurements of either the number size distribution or the particle morphology.

Introduction

Several recent computational studies have underlined that small, wavelength-sized ice crystals with extreme aspect ratios, resembling needlelike or platelike particles, are characterized by unusual scattering properties.[1−3] Zakharova and Mishchenko,[1] for example, have used the T-matrix method to calculate the extinction efficiencies, asymmetry parameters, and phase matrix elements of randomly oriented prolate and oblate ice spheroids with aspect ratios down to 0.05 (prolate shape) and up to 20 (oblate shape). The refractive index of ice was set to 1.311, being representative of nonabsorbing, visible wavelengths. Limited by the increasing numerical instability of the T-matrix calculations for large aspherical particles, the computations were extended up to equal-surface sphere size parameters of 12. As a principal outcome, only the asymmetry parameters and phase functions of the needle- and platelike ice particles resembled those of more compactly shaped, surface-equivalent ice spheroids with aspect ratios of 0.5 and 2.0. The plots of all other elements of the phase matrix as a function of the scattering angle revealed a pattern characteristic of Rayleigh scatterers. For example, the ratio of the elements P22 and P11 of the phase matrix **P** was close to unity for all scattering angles. As a consequence, highly aspherical ice spheroids should reveal only a very weak back-scattering depolarization ratio. In addition, the extinction efficiencies of the needle- and platelike particles were several times lower than those of the moderately aspherical spheroids. As demonstrated by supplementary studies, these results do not only apply for habits with a smooth surface such as spheroids but are also typical of sharp-edged and faceted shapes such as circular disks[2] and elongated hexagonal columns.[3]

The habit diagram of ice crystals, summarizing the variation of the ice crystal morphology with temperature and supersaturation, includes several regimes where the growth of needle- and platelike ice crystals is favored.[4] For example, at temper-

* Author to whom correspondence should be addressed. E-mail: Robert.Wagner@imk.fzk.de.

10.1021/jp0741713 CCC: $37.00
Published on Web 11/16/2007

atures close to 258 K and relative humidities just below saturation with respect to supercooled water, ice crystals typically grow into thin platelike shapes.[5] In contrast, needlelike habits are encountered at 268 K and ice supersaturation levels above water saturation. Long needlelike columns were also frequently observed at lower temperatures between 223 and 203 K for ice supersaturations between 0.2 and 0.6.[6] Such needle- and platelike ice particle habits may therefore contribute to the wealth of different ice crystal habits that occur in natural ice crystal clouds such as cirrus[7] and noctilucent clouds.[8,9] As highlighted by Zakharova and Mishchenko, the exceptional extinction and scattering properties of these particle shapes should be considered when interpreting laboratory and remote-sensing measurements of light extinction and scattering.[1,2] In particular, the authors pointed out that ice crystal sizes retrieved from spectral measurements of extinction could be biased, given the strongly different extinction efficiencies of, on the one hand, needle- and platelike particles and, on the other hand, moderately aspherical particles. An illustrative example for exactly this effect will be given in the present paper, focusing on extinction measurements of ice clouds at midinfrared wavelengths.

Our investigations are part of ongoing research activities on ice nucleation at the AIDA aerosol and cloud chamber of Forschungszentrum Karlsruhe.[10] The AIDA chamber can be operated as an expansion cloud chamber to study the formation of ice clouds down to temperatures of about 183 K.[11] For the quantitative analysis of the ice nucleation experiments in terms of nucleation rates and ice activation spectra, it is essential to infer the absolute ice particle number concentrations (N_{ice}) in the course of an expansion experiment. In a recent study, we have analyzed how accurately this information can be retrieved from broadband extinction measurements in the midinfrared regime (6000−800 cm^{-1}).[12] To do so, we have retrieved the time-dependent number size distributions $n(D_i)$ as well as N_{ice} of the ice clouds from the recorded infrared spectra and have compared these data to independent measurements with various optical particle counters (OPCs). For the size distribution retrievals, the ice crystals were modeled as finite circular cylinders in random orientations, employing moderate aspect ratios in the range from 0.5 to 3.0 to calculate the extinction cross-sections with the T-matrix method. We have analyzed expansion experiments performed at temperatures between 195 and 238 K where the nucleated ice crystals grew to sizes of 1−15 μm (equal-volume sphere diameters), depending on the available water vapor concentration and the number concentration of preadded, ice-active seed aerosol particles. It turned out that the infrared retrievals were often subject to severe solution ambiguities; i.e., different size/shape combinations of ice crystals yielded the same extinction spectra, rendering it extremely difficult to deduce accurate information about the absolute ice particle number concentrations and ice crystal shapes. However, there was one conclusion regarding the ice crystal habits that could be inferred from the infrared spectra analysis, at the same time denoting the starting point of our current study. We have observed for almost all expansion experiments where small ice crystals with median equal-volume sphere diameters less than 6 μm were formed that the corresponding infrared spectra could be accurately reproduced for all chosen aspect ratios in the range from 0.5 to 3.0. Moreover, there was always a very good agreement between the deduced ice particle number concentrations and the independent OPC measurements. The spread in the retrieval results with respect to N_{ice} was about ±20% for the different shape parameters (see Table 1 in Wagner et al.[12]), being comparable to the uncertainty range of the OPC measurements. As a result, we were not able to assess whether, for example, thick ice plates (aspect ratio 2−3) or short ice columns (aspect ratio 0.5) were formed in the expansion. But our results demonstrated that within the broad range of different ice cloud formation conditions that were covered by our experiments (temperature range from 238 to 195 K, critical ice supersaturations ranging from a few percent up to 70% depending on the employed seed aerosol particles) moderately aspherical particle habits were primarily formed. To arrive at this conclusion, we must remember the theoretical results by Zakharova and Mishchenko.[1,2] Suppose that highly aspherical, needle- or platelike ice crystals had formed during an expansion experiment. Then it is reasonable to assume that neither their infrared spectra could be accurately fitted employing moderate aspect ratios nor that the so-retrieved N_{ice} data would agree with the independent OPC measurements. A recent set of AIDA expansion experiments, performed during a measurement campaign in fall 2005, hereafter referred to as the IN07 campaign, enables us to check these postulations.

The experiment series was dedicated to study the influence of coating layers on the efficiency of deposition ice nucleation on mineral dust particles. As a dust sample, the claylike mineral Illite was employed; the coating layer was made of secondary organic matter generated by the ozonolysis of α-pinene at room temperature. We will show results from the following three different ice nucleation experiments: (i) ice nucleation on pure Illite particles; (ii) ice nucleation on pure secondary organic aerosol (SOA) particles (generated by reacting α-pinene with ozone in the absence of Illite particles); (iii) ice nucleation on SOA-coated Illite particles (generated by reacting α-pinene with ozone in the presence of Illite particles as seed aerosol). All experiments were performed at a temperature of 210 K; the median equal-volume sphere diameters of the generated ice crystals were in the range from 4 to 6 μm. Experiments i and ii have confirmed our previous conclusions; for experiment iii, however, we have observed for the very first time a large discrepancy between the N_{ice} values measured with the OPCs and those deduced from the infrared spectra when assuming moderately aspherical particle shapes in the retrieval. Just for experiment iii, we have detected an exceptionally low backward depolarization ratio at a wavelength of 488 nm, its value almost equalling the background value measured in the case of non-depolarizing spherical particles. Such a low depolarization ratio can only be explained by the presence of highly aspherical particle habits. We have therefore extended our analysis of the infrared spectra and have computed the infrared extinction cross-sections of micron-sized ice cylinders also for much larger aspect ratios, extending up to 10 for oblate shapes and down to $^1/_6$ for prolate shapes. Indeed, the incorporation of these highly aspherical particle habits in the retrieval of the ice particle number size distributions leads to a much better agreement of the deduced N_{ice} values with the independent OPC measurements. Experiment iii thus represents an impressive example to underline the predictions of Zakharova and Mishchenko.[1,2] The possibility that plate- or needlelike particles are present should therefore always be taken into account when deriving size distributions from spectral measurements of extinction.

We will present our current findings in the following order: In section 2, we will briefly introduce the methodology of the AIDA expansion experiments before addressing in detail the expansion runs from the IN07 campaign with the three different seed aerosol types (section 3). From the interplay of various measurement techniques, it will become apparent that in experiment iii strongly aspherical ice crystals have formed. In

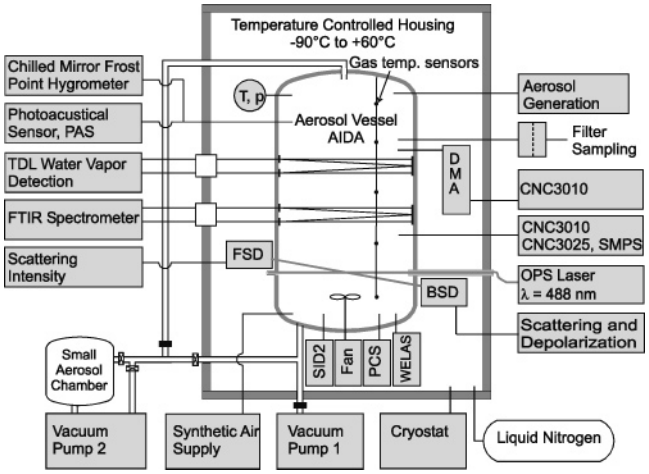

Figure 1. Schematic view of the AIDA aerosol chamber facility, featuring the relevant instrumentation for the expansion cooling experiments.

section 4, we will then present the results of our calculations of the infrared extinction cross-sections of ice crystals with a high degree of particle asphericity, using both the T-matrix method and the discrete dipole approximation (DDA) as computational tools. Finally, we will show in section 5 that it is necessary to include these extreme aspect ratios in the infrared retrieval procedure to reconcile the so-derived ice crystal number size distributions and total number concentrations with the OPC reference measurements.

Methods

A schematic cross-section of the AIDA aerosol chamber facility, featuring the major scientific instrumentation used for the ice nucleation studies, is shown in Figure 1.

The 84 m^3 sized, evacuable aluminum aerosol vessel is positioned inside an isolating containment whose interior can be cooled to a temperature as low as 183 K. After temperature equalization, the inhomogeneity throughout the entire vessel, monitored by arrays of horizontally and vertically arranged temperature sensors, is less than ± 0.3 K. In preparation for an expansion cooling cycle, the following steps have to be performed: (i) Evacuation of the chamber to <0.1 hPa, followed by flushing cycles with particle-free synthetic air to establish background particle concentrations of less than 0.1 cm^{-3}. (ii) Refilling the chamber with humidified synthetic air to 1000 hPa at a higher temperature (typically about 268 K) and subsequent cooling to the temperature that was chosen as the starting temperature for the ice nucleation experiment. Upon cooling, the excess water vapor forms a thin ice layer on the chamber walls, meaning that an expansion cycle is started at an ice saturation ratio $S_{ice} = p_w(T)/p_{w,ice}(T)$ close to one; the water vapor pressure, $p_w(T)$, is roughly equal to the saturation water vapor pressure over ice, $p_{w,ice}(T)$. (iii) Preparation and addition of the desired seed aerosol particles. At this time, the mixing fan, located at the bottom of the aluminum vessel, is switched on. Its operation not only further reduces the temperature inhomogeneities to ± 0.2 K but also provides for homogeneous conditions in terms of the aerosol and cloud particle number concentration and size throughout the chamber volume.

To initiate the ice cloud formation, the AIDA pressure is reduced by controlled pumping, typically from 1000 to 800 hPa within 4−10 min, leading to maximum cooling rates of about 4−0.1 K min^{-1}. During pumping, p_w at most linearly decreases with the total pressure, whereas $p_{w,ice}$ exponentially decreases with decreasing gas temperature. Thereby, ice supersaturated conditions with S_{ice} well above 1.6 can be established inside the chamber. Ice nucleation comes about when the temperature-dependent critical threshold relative humidity for the preadded seed aerosol particles is exceeded. The p_w time profile during the expansion cycle as well as the properties of the generated ice clouds are probed with a broad variety of complementary measurement techniques, as will be briefly outlined in the following.

In Situ Tunable Diode Laser Water Vapor Absorption Spectroscopy. The laser beam from a near-infrared tunable diode laser (TDL) is coupled via an optical fiber into one of the three individual, horizontally aligned White-type multiple reflection cells that are located at medium height of the aerosol vessel; see Figure 3a in Wagner et al.[12] By modulating the laser current, the entire line profile of a selected rovibrational water vapor absorption line in the 1368−1372 nm wavelength range is scanned to selectively derive the interstitial water vapor concentration even in the presence of condensed-phase water containing aerosol and/or cloud particles with an estimated uncertainty of $\pm 5\%$.[13] The TDL system provides a time resolution of about 1.5 s.

In Situ Fourier Transform Infrared Extinction Measurements. By coupling a Fourier transform infrared (FTIR) spectrometer (type IFS 66v, Bruker) to one of the White cells at level two of the AIDA chamber, infrared extinction spectra can be recorded in situ with optical path lengths of up to 250 m. The infrared White cell is equipped with BaF_2 cell windows, their transmittance confining the measurements to the 6000−800 cm^{-1} spectral range. During an expansion cycle, the infrared spectra are typically recorded at a rate of 6 spectra/min with 4 cm^{-1} resolution. The extinction spectra are analyzed using the T-matrix method to retrieve the number size distributions and total ice particle number concentrations of the generated ice clouds. A comprehensive description of the experimental setup as well as the retrieval procedure is given by Wagner et al.[12] Here, we want to briefly address a potential perturbation of the FTIR extinction measurements that is related to the fact that the mirrors of the infrared White cell are underlain with heating foils to keep their surface temperature about 10 K above the gas temperature and thus prevent them from icing.[12] So, there exists a small transition layer between the mirror surfaces and the well-mixed part of the chamber volume where the bulk flow and temperature patterns will be different from those of the well-mixed gas volume. Ice particles that are drawn past the mirrors near their surfaces will momentarily experience a lower ice saturation ratio compared to the particles within the well-mixed chamber interior. With a horizontal line of five temperature sensors mounted close to the aluminum walls of the AIDA chamber, we have measured a thickness of less than 10 cm for the transition layer between the vertical vessel walls and the mixed part of the gas volume.[14] We expect a similar transition layer thickness also for the mirror surfaces. Taking into account that the base length of the multiple reflection cell is 380 cm, the transition layer thickness corresponds to less than 5% of the total optical path length of the extinction measurements. In view of the much larger uncertainties in deriving accurate ice particle number concentrations from infrared extinction measurements associated with the problem of finding an appropriate shape representation for the aspherical particle habits, this small disturbance of the extinction measurements will be neglected.

As in our precedent study, the recorded infrared spectra will be treated as pure ice spectra, thus neglecting the small, submicron-sized inclusions of the seed aerosol particles within

the ice crystals. In a previous model calculation, we have demonstrated that a dust inclusion of 0.5 μm in diameter centered within a 5 μm sized cloud droplet does not change its extinction coefficients by more than $\pm$3% at wavenumbers between 6000 and 800 cm^{-1}; see Figure 4 in Wagner et al.[15]

In Situ Laser Light Scattering and Depolarization Measurements. At level one of the AIDA chamber, the laser beam of an optically pumped semiconductor (OPS) laser (emission at 488 nm, >100:1 vertical polarization) is directed horizontally through the AIDA chamber and is caught by a beam trap at the opposite chamber wall. The polarization plane of the incident laser light can be aligned parallel or perpendicular to the scattering plane using a combination of a quarter-wave plate and a thin film polarizer. Scattered light is detected in a near forward direction (scattering angle 2°) and polarization-resolved in a near backward direction (scattering angle 178°). A Glan-Laser polarization prism with two exit windows is used to split the back-scattered light into the parallel and perpendicular components with respect to the initial polarization plane. These components are detected by two independent photomultiplier tubes operating in the photon counting mode with 1 s integration time. With I_{par} and I_{per} denoting the background-corrected back-scattered intensities measured in the two channels, we define the depolarization ratio δ as $\delta = I_{per}/I_{par}$.

Optical Particle Counter WELAS. The optical particle counter WELAS (Palas GmbH, Germany) operates in an ex situ sampling mode but is mounted inside the cold containment at the bottom of the AIDA chamber to minimize the evaporation of ice crystals; the chamber air is sampled through a strictly vertical tube of 100 cm in length and 1 cm in inner diameter at a flow rate of typically 5 L/min. The overall internal volume of the sampling tube and of the WELAS measurement cell amounts to about 0.08 L and is therefore purged within 1 s. This small temporal offset compared to the in situ FTIR measurements will be neglected in our analysis. The OPC-WELAS measures the intensity of white light scattered by single particles into scattering angles from 78° to 102° for particle counting and sizing.[16] Accurate particle number concentrations with an estimated uncertainty of $\pm$20% are obtained from the single particle count rate and the sampling flow through the optical detection volume. For a refractive index of 1.3 at visible wavelengths, only particles larger than about 0.8 μm in diameter can be detected. Only for the expansion cooling cycles at very low temperatures (<200 K) a significant fraction of the nucleated ice crystals might remain in the submicron size range due to the low water vapor concentration, which is available for the ice crystal growth; see, for example, Figure 10 in Wagner et al.[12] Otherwise, the generated ice clouds will be fully mapped by WELAS; to selectively derive N_{ice}, however, it is necessary to subtract the fraction of unactivated seed aerosol particles that is visible to WELAS from the total particle count rate; see Figure 2 in Wagner et al.[12] Note that accurate sizing by WELAS is only accomplished for spherical particles; for aspherical ice crystals the deduced particle "diameters" can only be interpreted as "apparent" sizes because the detector response depends on the accidental orientation of the particles in the detection volume.

Comparability of the FTIR Extinction and OPC-WELAS Measurements. When using the optical particle counter WELAS as a reference sensor for the retrievals of the ice particle number concentrations from the FTIR extinction spectra, we have to ensure that the ice cloud properties are sufficiently homogeneous throughout the chamber volume so that the measurements from these two probes can be directly compared, given that their locations are completely different: The OPC-WELAS operates in an ex situ mode by sampling chamber air from a distant point near the bottom of the chamber, whereas the FTIR extinction spectra are recorded in situ at medium height of the chamber volume. We have already briefly addressed this issue in our previous work[12] but want to summarize below further evidence from the intercomparison of different AIDA measurement techniques that also our ex situ probes provide representative microphysical properties of micron-sized cloud particles to which the retrieval results from the in situ infrared measurements can be compared.

(i) AIDA expansion experiments that were performed at temperatures above 235 K and resulted in the formation of pure clouds of supercooled water droplets provide a valuable check for the comparability of the FTIR extinction and OPC-WELAS measurements. First of all, the FTIR analyses are not affected by simplifying assumptions on the shape of the cloud particles. Instead, the application of Mie theory in combination with accurate infrared refractive index data sets for supercooled water will allow for a unique retrieval of the number size distributions of the spherical cloud droplets.[15] Second, using Mie theory for the analysis of the OPC-WELAS recordings will also enable proper sizing of the cloud droplets in addition to measuring their number concentrations. As stated in Wagner et al.,[12] we have always observed good agreement between the cloud droplet diameters deduced from the FTIR retrievals and the OPC-WELAS measurements; see Figure 5 in Benz et al.[16] and Figure 13 in Wagner et al.,[15] addressing AIDA expansion experiments with supercooled H_2SO_4/H_2O solution droplets as seed aerosol particles, started at $T = 243$ K. Within the 20% uncertainty range of the OPC-WELAS, the two different measurement techniques also agreed with respect to the number concentrations of the water droplets, which have formed during such types of expansion experiments. As a further check, the maximum droplet number concentrations during the expansion experiments agreed to $\pm$20% with the number concentrations of the preadded sulfuric acid droplets, measured with a condensation particle counter (CPC3010, TSI) that samples chamber air form a distant point in the upper part of the chamber volume (Figure 1). Thus, three completely independent measuring techniques, each involving a different location in the AIDA chamber, provide consistent data with respect to the number concentrations of the micron-sized cloud particles, thereby underlining the appropriateness of using the OPC-WELAS as a representative sensor for N_{ice} in our present experiments.

(ii) During several AIDA measurement campaigns two different optical particle counters and an additional laser scattering device (the small ice detector (SID)) were used to measure the number concentrations of the nucleated ice crystals. The instruments were connected to the chamber volume by independent sampling tubes, thus probing different parts of the chamber interior.[10,12] The intercomparisons of the measured ice particle number concentrations shown in Figures 3 and 4 in Möhler et al.[10] reveal good agreement between the various instruments, emphasizing that the potential spatial fluctuations of N_{ice} within the chamber volume are not significantly larger than the estimated uncertainty ranges of the measuring instruments.

(iii) We have always observed good agreement between the two different methods for measuring the overall ice water content (IWC) of the ice clouds that have formed during the AIDA expansion experiments. First, the IWC can be reliably retrieved from the FTIR extinction spectra because different assumptions on the shape of the ice crystals usually do not affect the retrieved ice volume concentrations by more than $\pm$10%.[12]

TABLE 1: Parameters of AIDA Expansion Experiments from the IN07 Measurement Campaign

experiment	sample	p (hPa)	T_{gas} (K)	N_{ae} (cm^{-3})	pump
IN07_19	Illite	1001.3	209.8	116	60%
IN07_20*	Illite	1005.8	210.1	78	60%
IN07_26	SOA	1003.9	211.3	5660	80%
IN07_27*	SOA	1004.0	211.3	4200	80%
IN07_28	SOA	1002.2	211.4	3060	60%
IN07_22	Illite + SOA	999.1	210.4	122	60%
IN07_23*	Illite + SOA	997.8	210.5	90	60%
IN07_24*	Illite + SOA	998.0	210.6	70	80%

Second, the IWC can be inferred from the difference of the total water mixing ratio, i.e., the sum of interstitial water vapor and evaporated ice crystal water, and the interstitial gas-phase water concentration. The first quantity was measured with either a fast scanning chilled mirror hygrometer (LX-373, MBW) or the Lyman-α-fluorescence hygrometer FISH;[17] both techniques sampled chamber air from the upper part of the chamber volume through a heated inlet tube where all ice crystals completely evaporated. The second quantity was measured in situ at medium height of the AIDA vessel by tunable diode laser absorption spectroscopy, as described above. Figure 4 in Wagner et al.[11] and Table 1 in Mangold et al.[17] show a comparison between these independent IWC measurements in the AIDA chamber, revealing that they do not differ by more than ±20%.

Experimental Results From the IN07 Campaign

Table 1 lists the parameters of the AIDA ice nucleation runs of the IN07 campaign from October 2005, which were analyzed for the present study. All experiments were started at an initial pressure p close to 1000 hPa and at an initial gas temperature T_{gas} of about 210 K. For each seed aerosol sample, two or three repeated cooling cycles were performed; i.e., the chamber was refilled to 1000 hPa after the complete evaporation of the ice crystals, and another expansion was started with the remaining seed aerosol loading. The seed aerosol particles were first prepared and characterized inside the smaller, 4 m^3 sized aerosol vessel to the left of the main vessel (Figure 1) before injecting them into the AIDA chamber. The initial seed aerosol number concentrations N_{ae} inside the AIDA vessel ranged from 70 to 5660 cm^{-3}, as measured with a condensation particle counter (CPC3010, TSI). The median volume-equivalent sphere diameters of the seed aerosol particles, measured with a scanning mobility particle sizer (SMPS, TSI) and an aerodynamic particle sizer (APS3321, TSI), were about 0.4 μm for the Illite particles and about 0.2 μm for the pure secondary organic aerosol particles formed by the α-pinene + O_3 reaction. For the aspherical Illite particles, the measured mobility and aerodynamic diameters were converted into equal-volume sphere diameters using a particle density of 2.5 g/cm^3 and a dynamic shape factor of 1.5. Upon coating the Illite particles with secondary organic matter, an about 20−25% increase of the median volume-equivalent sphere diameter was detected. Here, best agreement between the SMPS mobility and the APS aerodynamic diameter was achieved with a particle density of 2.0 g/cm^3 and a dynamic shape factor of about 1.2. From this we can estimate a SOA volume fraction of about 40−50% for the SOA-coated Illite particles. The shape factor of 1.2 indicates that the particles are still of an aspherical shape, as also concluded from the depolarization measurements; see below. The final column in Table 1 lists the pumping speeds that were applied for the expansions, expressed as a fraction of the maximum rotary speed of the mechanical pump. Marked by asterisks are the expansion cycles for which detailed time series of the various AIDA data are plotted in Figure 2.

The contents of Figure 2 are arranged in the following order. The top row panels show the time evolutions of the saturation ratios with respect to ice and supercooled water in the course of the expansion experiments, obtained as quotients of the measured water vapor concentrations (TDL data) and the saturation water vapor pressures over ice and liquid water, calculated with the equations from Murphy and Koop[18] for the given mean AIDA gas temperature. The latter is calculated as the average of the measurements with the vertically oriented array of thermocouple sensors shown in Figure 1. Time zero denotes the start of pumping, also marked by a vertical line in the time series plots. The second vertical line represents the onset time of ice nucleation. Note that the higher pumping speeds that were applied in the expansions IN07_27 and IN07_24 initially lead to a faster rise of the saturation ratios, dS_i/dt, compared to experiments IN07_20 and IN07_23.

The original scatter plots from the optical particle counter WELAS are shown in the second row. Each dot features a single particle count event in one of the OPC size channels. The small-sized SOA particles used in experiment IN07_27 do not extend into the measurement range of the OPC; i.e., the total OPC count rate directly equals the ice particle number concentration N_{ice}. As for the expansions IN07_23 and IN07_24, it is feasible to introduce a threshold size to separate the ice crystal mode from the fraction of SOA-coated Illite particles that are visible to the OPC. In the case of experiment IN07_20, the interfering dust particles were subtracted using eq 2 from Wagner et al.[12] to deduce N_{ice} from the overall OPC count rate.

In row three of Figure 2, we show the results from the polarization measurements with the laser light scattering device. Black lines represent the back-scattered intensities I_{par}, and gray lines represent I_{per}. In expansion IN07_27, the polarization plane of the incident laser beam was rotated to be perpendicular to the scattering plane for the time period between 580 and 820 s to demonstrate the good compensation of the two photomultiplier channels. Time series of the depolarization ratios calculated from I_{par} and I_{per} are plotted in the fourth row. The bottom row panels depict time series of the infrared extinction spectra that were recorded during the expansion experiments, nicely reflecting the continuous growth of the nucleated ice crystals. In contrast to the large volume density of ice that is formed in each expansion cycle, the volume concentrations of the preadded seed aerosol particles are too low to be detected in the infrared spectra. The time periods covered by the spectra recordings are indicated by gray horizontal bars on the time scales in row four. With respect to their temporal order, the spectra are to be read from bottom to top. For a matter of clarity only every second recorded spectra is plotted; i.e., the time interval between two depicted measurements is 20 s. Note that for expansions IN07_27 and IN07_23 scaling factors of 1.5 and 0.5 for the extinction coefficients are introduced.

We will begin our analysis by comparing the ice particle number concentrations measured by the OPC with those obtained from the FTIR retrievals for the expansion cycles IN07_20 and IN07_27. The results are shown in Figure 3, using the graphical representation that we have already applied in our previous work;[12] see, for example, Figure 8 therein. Gray dots designate $N_{ice}(t)$ from the OPC records; 20% error bars are included. For retrieving the ice particle number size distributions from the infrared spectra, the ice crystals were modeled as pure or shape-averaged finite circular cylinders with aspect ratios ϕ, i.e., the ratios of the diameter to the length of the cylinders, in

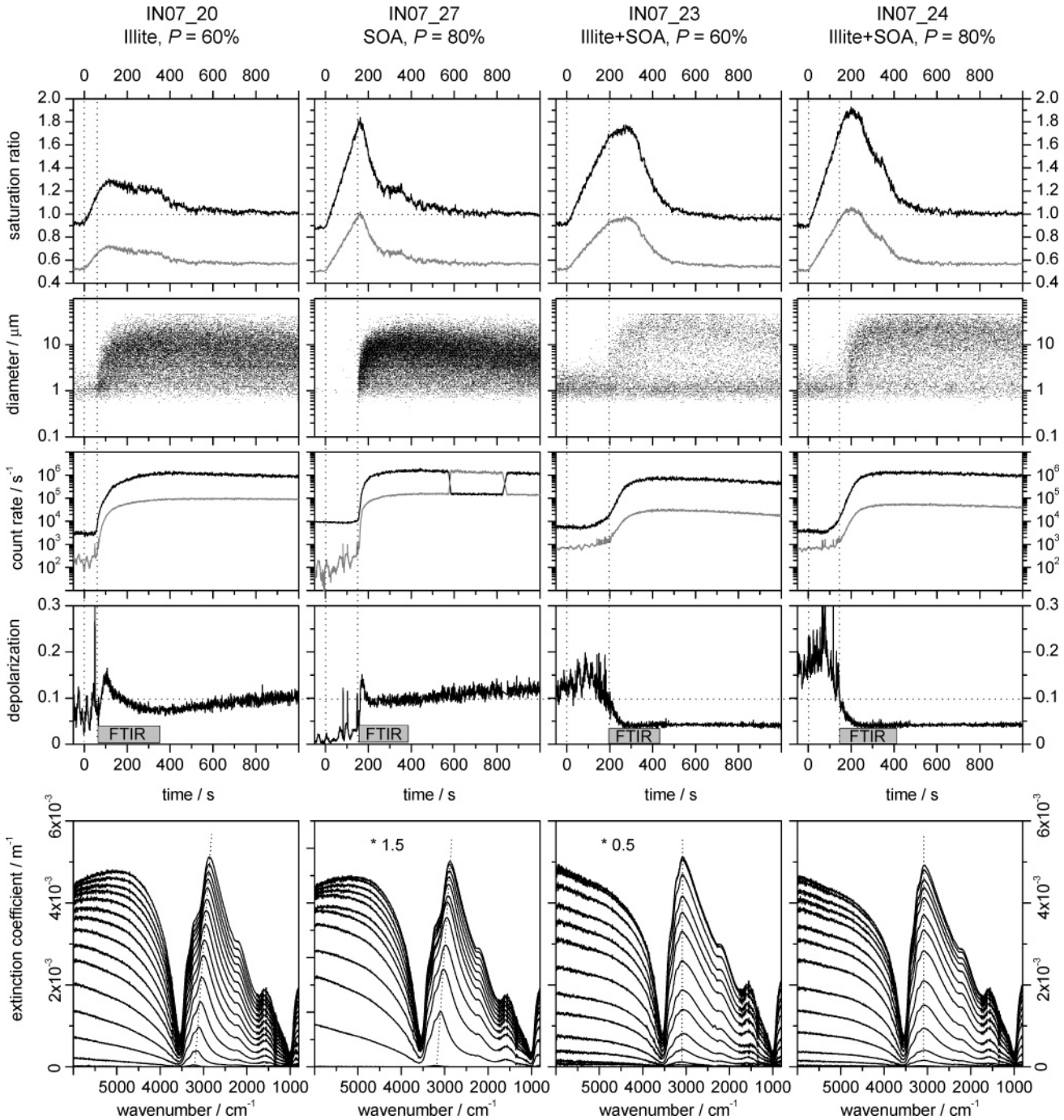

Figure 2. Panels 1−4: Time series from expansion cycles IN07_20, IN07_27, IN07_23, and IN07_24. Panel 1: Saturation ratios with respect to ice (black lines) and supercooled water (gray lines). Panel 2: Size of individual particles detected by the OPC-WELAS. Panel 3: Polarization-resolved back-scattering intensities I_{par} (black lines) and I_{per} (gray lines) from the laser light scattering device. Panel 4: Back-scattering depolarization ratio δ. Panel 5: FTIR extinction spectra recorded at different times during the expansion cycles. See text for details.

the range from 0.5 to 3.0. For each of altogether 126 shape distributions, the ice crystal number size distributions were retrieved assuming unimodal log-normal distribution functions. As discussed in Wagner et al.,[12] we consider the unimodal log-normal constraint as a justified and necessary simplification for the reliable determination of the ice particle number concentrations. When employing an algorithm that allows multimodal particle size distributions, pseudo-modes of smaller and larger ice particles might emerge even if the true number size distribution is unimodal. This is because the additional degrees of freedom in the multimodal retrieval provide an opportunity to repair the mismatch between the measured and the calculated extinction spectrum that is induced by slightly inaccurate optical constants and/or an approximated particle shape representation for the ice crystals. All ice nucleation experiments that are analyzed in the following were performed with a single type of aerosol particles as ice nuclei, leading to a single nucleation event at a specific threshold relative humidity and a single-mode distribution of ice crystals, as documented by the scatter plots from the optical particle counter WELAS shown in Figure 2. Note that we do not report experiments where different types of aerosol species with different threshold relative humidities for ice nucleation were employed. Such experiments could indeed lead to dual or multiple nucleation events and concomitantly bi- or multimodal ice crystal size distributions, as shown, for example, in Figure 15 of Wagner et al.[12]

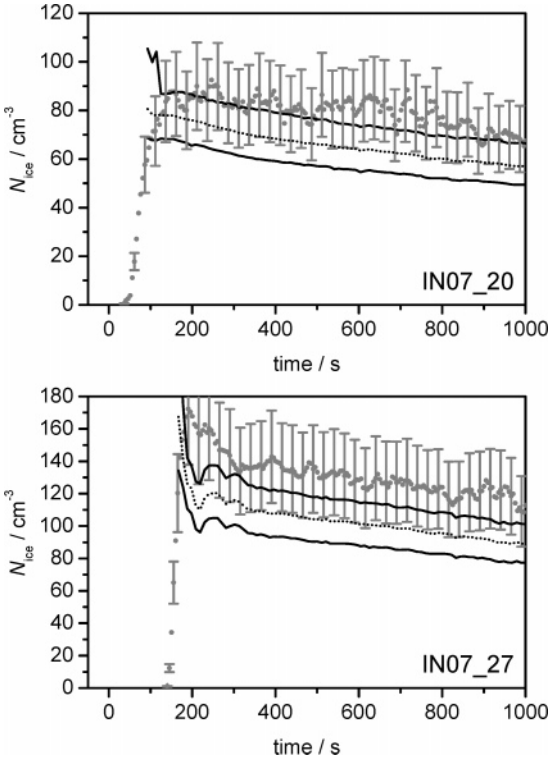

Figure 3. Time series of the ice particle number concentrations N_{ice} for expansion experiments IN07_20 and IN07_27 derived from the OPC-WELAS recordings (gray) and the FTIR extinction measurements (black). See text for details.

In each panel of Figure 3, the two solid black lines represent envelopes of the highest ($N_{ice,max}$) and lowest ($N_{ice,min}$) ice particle number concentrations within the set of considered shape distributions; $N_{ice}(t)$ averaged over all different shape assumptions is designated by dotted black lines. Note that we have omitted the initial time period of the ice nucleation event in the plots of the FTIR retrieval results. As long as the freshly nucleated ice crystals are still smaller than 1.5 μm in diameter, the infrared analysis only allows for a unique retrieval of the ice volume concentration but not of the individual parameters of the log-normal size distribution.[12]

In the course of the expansion cycles IN07_20 and IN07_27, the ice crystals grew to median sizes (expressed as equal-volume sphere diameters D_V) of 4.9 and 4.7 μm. In accordance with our previous findings, the $N_{ice}(t)$ data inferred from the OPC are properly reproduced by the FTIR results when applying moderately aspherical particle shapes in the retrieval. As for IN07_20 and IN07_27, the OPC data tend to agree better with the upper half of the spectrum of infrared retrieval results spanned by $N_{ice,max}$ and $N_{ice,min}$. These higher ice particle number concentrations are obtained from the fits with the most compact shape parameters within the considered range of aspect ratios; see Table 1 in Wagner et al.[12] An equally good agreement between the $N_{ice}(t)$ data deduced from the two different techniques was also observed for the other expansion cycles with pure Illite and SOA seed particles (IN07_19, IN07_26, and IN07_28). Note that for these two different seed aerosol types the initial ice crystal growth has been subjected to quite diverse ice saturation ratio profiles. The Illite particles act as ice nuclei at a very low critical ice saturation ratio of 1.1 with almost 100% efficiency. The peak relative humidity with respect to ice in the course of expansion IN07_20 only reached a value of 130%. In contrast, 100% relative humidity with respect to supercooled water (180% with respect to ice) was approached before the onset of ice nucleation on the SOA particles occurred. These two expansions thus support our statement from Wagner et al.:[12] For small ice particle sizes, predominantly rather compact crystal habits are observed for growth times on the order of a few minutes, notwithstanding the broad range of different ice cloud formation conditions that are covered by the AIDA expansion experiments. For the very first time, however, a different observation has been made for the expansion cycles IN07_22−24.

From the top row of Figure 2, it becomes evident that the time series of the saturation ratios for the expansions with SOA-coated Illite particles are similar to those observed for the pure SOA particles. The highly ice-active Illite particles are strongly deactivated by the organic coating; ice nucleation does not occur before 100% relative humidity with respect to supercooled water is reached. As a result of the higher pump speed that was applied for expansion IN07_24 compared to that for IN07_23, an optically thicker ice cloud with a higher ice particle number concentration was formed in this experiment. A first indication for the peculiarity of these expansion cycles comes from the exceptional spectral habitus of the infrared extinction spectra of the generated ice clouds. For very small ice crystals with negligible light scattering at infrared wavelengths, light extinction (in this case absorption) peaks at 3250 cm^{-1}, corresponding to the maximum of the intense O−H stretching absorption band. As can be observed from the spectra series for experiments IN07_20 and IN07_27 (highlighted by dotted lines), the peak extinction gradually shifts to lower wavenumbers as the ice crystals grow and the scattering contribution to the overall extinction spectrum increases. For the expansion cycles IN07_23 and IN07_24 (just as for IN07_22, not shown in the figure), however, the position of the extinction maximum does not change during ice crystal growth. As a result, the extinction spectra bare a distorted spectral habitus compared to those recorded during IN07_20 and IN07_27 and all other spectra series recorded so far (see, for example, Figure 8 in Wagner et al.[12]), especially in the regime of the O−H stretching mode.

In Figure 4, top panel, we compare a selected infrared extinction spectrum from the IN07_23 series, recorded at t = 447 s, with the best T-matrix fit result for cylindrical ice crystals of aspect ratio 0.7 (solid gray line). In spite of the spectral distortions discussed above, the measured spectrum is closely matched by the fit. The remaining small spectral deviations of up to 10% between the measured and the calculated extinction spectrum can easily be explained by the limited accuracy of the employed optical constants (estimated uncertainties of 1.5−4%)[19] and the other approximations in the retrieval procedure (e.g., log-normal constraint and assumption of a cylindrical ice crystal shape).[12] But the retrieval result for the ice crystal number size distribution is completely at odds with the OPC recordings. The T-matrix fit yields an ice particle number concentration N_{ice} of 181 cm^{-3}, a count median diameter D_V of 1.77 μm, and an unusually large mode width σ_g of 1.81. Usually, the mode width of the size distribution of the freshly nucleated ice particles rapidly narrows during the ice crystal growth by water vapor deposition; see, for example, Figure 8 in Haag et al.[20] In the course of the expansion cycles IN07_20 and IN07_27, for example, the retrieved mode widths quickly dropped to values below 1.2.

Moreover, as illustrated by the lower panel of Figure 4, the retrieved ice particle number concentrations for ϕ = 0.7 as well as for all other aspect ratios between 0.5 and 3.0 are more than 1 order of magnitude higher than the OPC reference measurements. At t = 447 s, for example, the OPC detects an ice particle

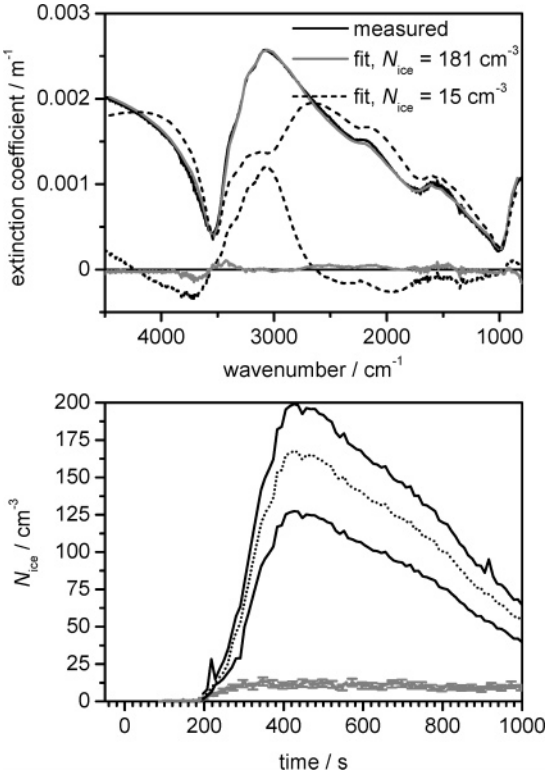

Figure 4. Top panel: Infrared extinction spectrum of ice crystals recorded at $t = 447$ s during expansion cycle IN07_23 (solid black line) in comparison with two T-matrix fit results for cylindrical ice crystals of aspect ratio $\phi = 0.7$. Solid gray line: Best fitted spectrum by independent optimization of the ice particle number concentration, the mode width, and the count median diameter. Dashed black line: Best fitted spectrum when fixing N_{ice} to 15 cm^{-3} and optimizing only σ_g and D_V. The same line types are used to plot the spectral residuals (differences from the measured spectrum) for both fit scenarios. See text for details. Bottom panel: Time series of the ice particle number concentrations N_{ice} for expansion experiment IN07_23 derived from the OPC-WELAS recordings (gray) and the FTIR extinction measurements (black), same representation as in Figure 3.

number concentration of 12.5 ± 2.5 cm^{-3} whereas N_{ice} data ranging from 123 to 193 cm^{-3} are obtained from the FTIR retrievals. These values are even higher than the number concentration of the preadded seed aerosol particles (90 cm^{-3}, measured with the CPC3010). A similar disagreement was also observed for the expansion cycles IN07_22 and IN07_24. Apparently, the FTIR retrievals fail for these expansion cycles if only moderately aspherical particle habits are allowed as input parameters. This is further emphasized by a second fit example shown as dashed black line in the top panel of Figure 4. Here, we have constrained the ice particle number concentration to 15 cm^{-3}, i.e., matching the upper error limit of the OPC record, and have only optimized the mode width and the count median diameter of the ice crystal size distribution. The so-derived best fitted spectrum is unable to mimic the measured spectral habitus; within the O−H stretching regime, the differences between the measured and the calculated spectrum almost approach a factor of 2. This large deviation cannot be explained by inaccurate optical constants and other simplifications in the retrieval procedure. Instead, the fit example illustrates that when prescribing the ice particle number concentration to the OPC measurement in the fitting procedure a compact ice particle shape will not provoke the observed spectral habitus of the infrared extinction spectrum.

Independent evidence that ice crystals with a high degree of particle asphericity might have formed during IN07_22−24 comes from the results of the laser light scattering measurements. For the expansions IN07_20 and IN07_27, the generated ice clouds depolarize the incident laser light by a ratio of about 0.1. Note that for experiment IN07_20 the preadded aspherical dust particles already cause a depolarization similar in magnitude to that of the ice crystals that are formed later on by deposition nucleation onto these seed particles. In contrast, a depolarization ratio close to zero is detected for the SOA particles. A small background value of typically 0.03 is observed even when only spherical droplets are present in the chamber. This is due to (i) Raleigh scattering by air molecules, (ii) an imperfect alignment of the Glan-Laser prism with respect to the initial polarization planes, (iii) a less than 100% horizontal or vertical polarization of the laser light, and (iv) an insufficient correction of background light reflected from the chamber wall. The depolarization ratio of the SOA-coated Illite particles in experiments IN07_23 and IN07_24 is even higher compared to pure Illite particles, underlining that the thin coating layer preserves the overall aspherical particle morphology, as also concluded from the APS measurements. But surprisingly, as soon as the ice clouds are formed during the expansion cycles IN07_23 and IN07_24, the depolarization ratio drops to a value of about 0.04, i.e., almost meets the background value detected for spherical particles. Considering the theoretical results from Zakharova and Mishchenko[1] (see middle column of Figure 2 therein), such a weak back-scattering depolarization ratio of micron-sized ice crystals will not be provoked by moderately aspherical particle habits. Instead, it is typical of needle- or platelike particles.

This supporting information that highly aspherical ice crystals might have formed during IN07_22−24 prompted us to perform a test calculation to evaluate whether the spectral distortions, observed for the infrared extinction spectra of the ice crystals in these experiments, can really be reproduced by considering higher aspect ratios in the T-matrix calculations. Our results are shown in Figure 5.

The top-left panel of Figure 5 depicts the infrared extinction cross-sections for cylindrical ice crystals of aspect ratio 1 for equal-volume sphere diameters ranging from 1 to 5.05 μm. The gradual red shift of the peak extinction in the O−H stretching regime with increasing particle size nicely mimics the trend that we have detected in the spectra series of the expansion cycles IN07_20 and IN07_27. In contrast, when repeating the calculations for $\phi = 5$ (top-right panel), the position of the extinction maximum barely shifts, in agreement with the spectral behavior observed during experiments IN07_23 and IN07_24. A direct comparison between the calculated extinction spectra of 5.05 μm sized ice crystals of aspect ratios 1 and 5 is shown in the bottom left panel. Next to this graph, we have depicted two selected infrared spectra from the experiments IN07_20 and IN07_23. The spectral discrepancies between these two measured spectra are very similar to those between the two calculated spectra. This strongly supports the indication from the depolarization measurements that ice crystals with a higher degree of particle asphericity have formed during IN07_22−24. Nevertheless, the infrared spectra of these expansion experiments can be accurately fitted with compact shape parameters (Figure 4). Obviously, even for strongly aspherical ice crystals, the differences in the extinction cross-sections compared to compactly shaped particles can be efficiently leveled out by distorting the true number size distribution of the ice cloud. It is therefore highly advisable to cross-check infrared retrievals of the number size distribution of micron-sized ice crystals with independent measurements.

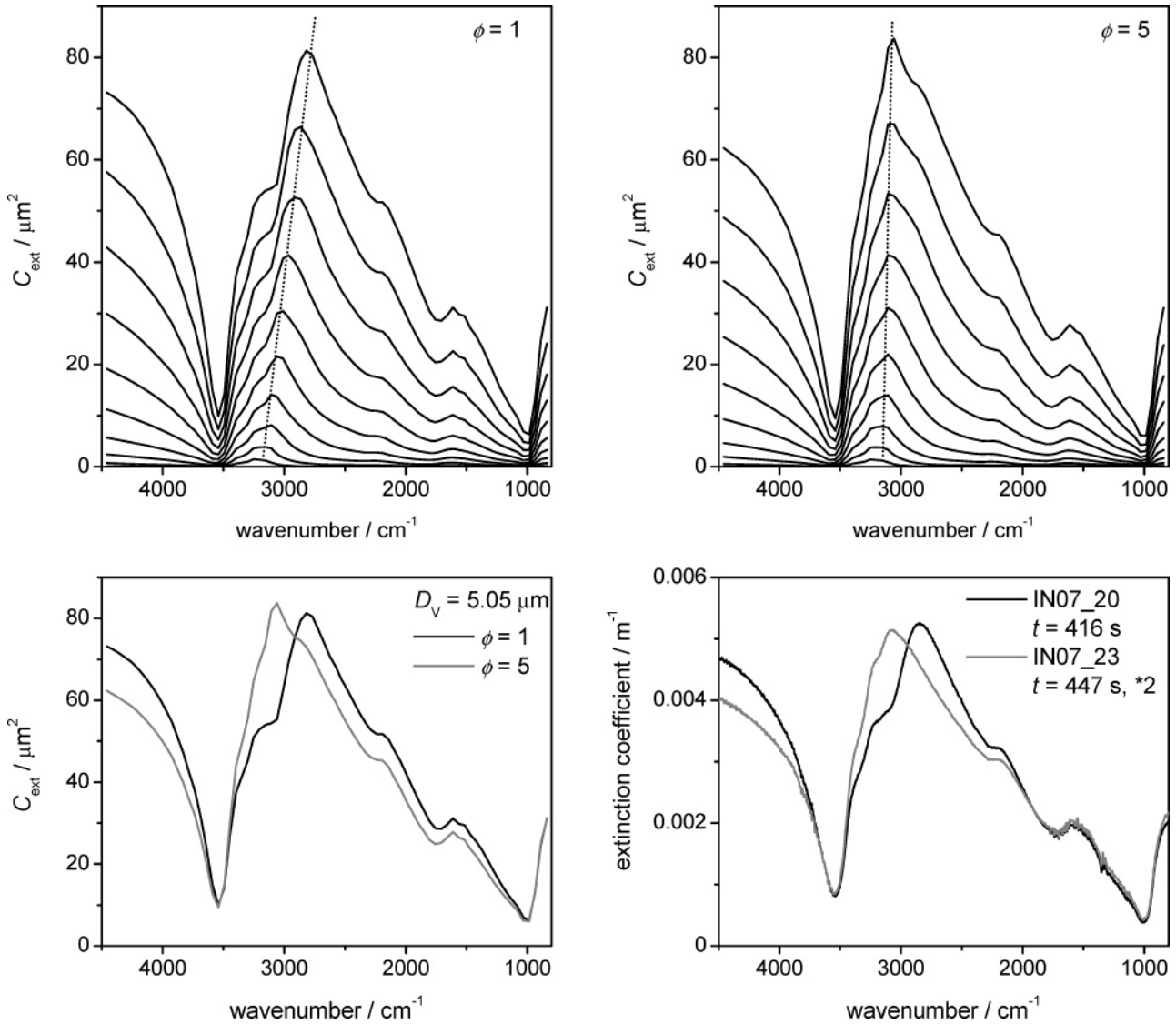

Figure 5. Top left panel: Extinction cross-sections (C_{ext}) of cylindrical ice crystals of aspect ratio $\phi = 1$ for equal-volume sphere diameters ranging from 1 μm (bottom spectrum) up to 5.05 μm (top spectrum) in 0.45 μm size steps. The top-right panel shows the same calculations for an aspect ratio of 5, i.e., platelike crystals. Bottom left panel: Comparison of the extinction cross-sections of 5.05 μm sized ice cylinders of aspect ratios 1 and 5. Bottom right panel: Comparison of two selected infrared extinction spectra of ice crystals generated in the course of expansion experiments IN07_20 and IN07_23. The spectrum recorded during IN07_23 (the same as in Figure 4) is scaled by a factor of 2.

As a further task for our present study, we want to investigate whether it is indeed possible to bring the OPC and FTIR data with respect to $N_{ice}(t)$ to a better match when considering strongly aspherical particle habits in the retrieval procedure. Before addressing this issue, we will focus in the next chapter on our supplementary calculations of the infrared extinction cross-sections of ice crystals with higher aspect ratios. These results will shed light on the origin of the shape-related distortions in the extinction spectra that are evident in Figure 5. Thereafter, we will repeat the infrared retrieval procedure for experiments IN07_23 and IN07_24, employing the newly calculated infrared extinction cross-sections of highly aspherical ice crystals.

Infrared Extinction Cross-Sections of Strongly Aspherical Ice Crystals

In our preceding study,[12] we have calculated the extinction cross-sections of circular ice cylinders with the extended precision FORTRAN T-matrix code for randomly oriented particles by Mishchenko and Travis[21] at 76 equidistant wavenumber points from 4500 to 800 cm^{-1} for equal-volume sphere diameters extending up to 25.0 μm. Five different aspect ratios, namely, $\phi = 0.5$, 0.7, 1.0, 2.0, and 3.0, were considered in these computations. In the present work, we have extended the range of aspect ratios up to 10.0 for oblate particle shapes (from $\phi =$ 4.0 to 10.0 in increments of 1.0) and down to $^1/_6$ for prolate shapes (individual calculations for $\phi = {}^1/_3$, $^1/_4$, $^1/_5$, and $^1/_6$). For a given size parameter, less aspherical particle habits are computable for columnlike cylinders compared to plates; see Tables 1 and 2 in Mishchenko and Travis.[21] For these more extreme aspect ratios, we have restricted the calculations to an upper particle size of $D_V = 10$ μm because otherwise too many T-matrix computations would have become nonconvergent. As will be evident from the fit results shown in the next section, this upper size limit is sufficient to map the major part of the number and volume size distributions of the ice clouds that have formed during the expansion experiments IN07_22−24, featuring narrow mode widths and median ice crystal diameters D_V of up to 6 μm. The extinction cross-sections were calculated for 67 discrete D_V values from 0.1 to 10.0 μm in 0.15 μm size

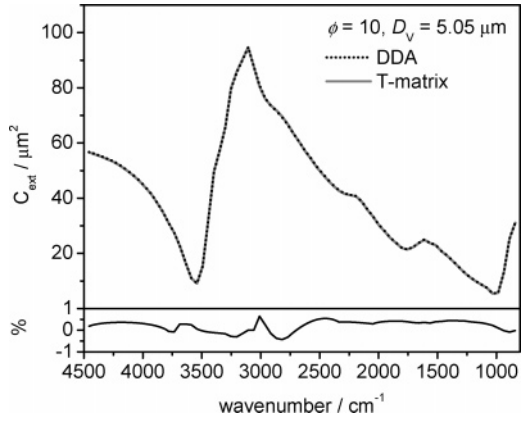

Figure 6. Top: Extinction cross-sections of finite circular ice cylinders with $\phi = 10$ and $D_V = 5.05$ μm in random orientation, calculated with the discrete dipole approximation and the T-matrix code. The percentage difference between the two computed spectra is shown in bottom panel.

steps, summing up to $76 \times 67 = 5092$ individual computations for each aspect ratio. Despite the reduced maximum ice crystal diameter, the T-matrix calculations did not converge for the entire range of particle sizes and wavenumbers. The more aspherical the particle shape, the more individual T-matrix calculations became nonconvergent. For example, 476 as well as 870 convergence errors appeared for $\phi = 9$ and $\phi = 10$; for $\phi = 1/6$, convergence was not obtained for 607 different particle size−wavenumber pairs. Convergence problems not only emerged for the highest size parameters but also in the regime of the intense O−H absorption band of ice at 3250 cm^{-1}, where the high imaginary part of the refractive index reduces the performance of the T-matrix code; see Table 3 in Mishchenko and Travis.[21] To complement our computations, we have calculated the extinction cross-sections for those particle size−wavenumber combinations where the T-matrix code failed to converge with the discrete dipole approximation (DDA), using the DDSCAT.6.0 FORTRAN software package.[22] Typically, arrays of about 25 000 dipoles were used to approximate the continuum cylindrical targets, satisfying the criterion that the interdipole separation should be small compared to any structural lengths in the targets. Again, the random orientation of particles was assumed. Note that DDA lacks an efficient procedure for orientational averaging, making it a time-consuming process as the extinction cross-sections have to be calculated separately for a sufficient number of different target orientations. For that reason, DDA was not used as the standard technique in the extinction calculations. To check the accuracy of the DDA results, we have compared them to the corresponding T-matrix computations for a particle size that does not yet lead to convergence problems. Figure 6 shows the DDA and T-matrix results for the wavenumber-dependent extinction cross-sections of ice cylinders with $\phi = 10$ and $D_V = 5.05$ μm, illustrating that both computations agree within ±1%.

Given that DDA can be applied to arbitrary particle geometries, we are also able to check that circular cylinders are indeed a reasonable surrogate for pristine hexagonal ice crystals in extinction calculations at infrared wavelengths − being an assumption from our previous study[12] which was based on the theoretical work by Lee et al.[23] Figure 7 demonstrates that the extinction cross-sections of randomly oriented circular ice cylinders (T-matrix results) and ice hexagons (DDA results) with the same aspect ratio ($\phi = 5$) and equal-volume sphere diameter ($D_V = 5.05$ μm) differ by less than ±3% over the complete wavenumber range. An equally good agreement was obtained for 5.05 μm sized particles of aspect ratios $\phi = 1$ and $\phi = 10$.

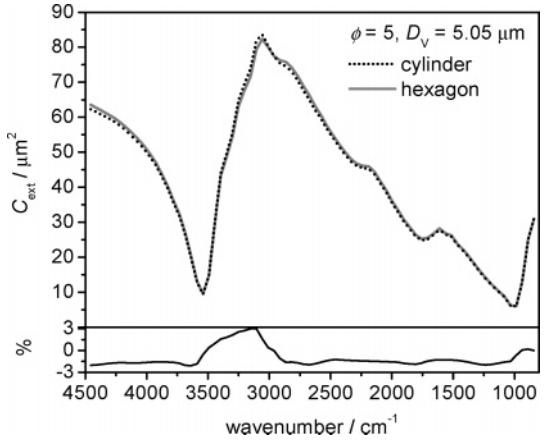

Figure 7. Top: Extinction cross-sections of randomly oriented finite circular ice cylinders and ice hexagons, both with $\phi = 5$ and $D_V = 5.05$ μm. The cylinder results were computed with the T-matrix code; the calculations for the ice hexagons were done with the discrete dipole approximation. The percentage difference between the two computed extinction spectra is shown in bottom panel.

As will be demonstrated below, these differences are very small compared to the changes in the extinction cross-sections that are induced by the variation of the aspect ratio of the circular ice cylinders.

As input for the T-matrix and DDA calculations, we employed low-temperature refractive indices of ice at 210 K, combining the data sets from Rajaram et al.[24] (4500−3700 cm^{-1}), Clapp et al.[25] (3700−1500 cm^{-1}), and Zasetsky et al.[19] (1500−800 cm^{-1}). The reason for using this combination of three different refractive index data sets is elaborated in our preceding publication.[12] The computations were run on an AIX cluster composed of several IBM pSeries machines.

Figure 8 compiles selected T-matrix results for the midinfrared extinction cross-sections of variously sized ice crystals as a function of increasing particle asphericity. For oblate particle shapes, the computed extinction spectra are shown for particle diameters D_V of 1.0, 3.1, 5.05, and 7.0 μm. For the two intermediate sizes, the C_{ext} spectra for prolate particle shapes are shown as a comparison. At first glance, the calculated extinction spectra for the smallest particle diameter of 1.0 μm show very little dependence on the particle shape; see also the recent computations by Zasetsky et al.[26] (Figure 7 therein). For example, the C_{ext} values for $\phi = 1$ and $\phi = 9$ at the 3250 cm^{-1} extinction maximum differ by only 2%. But, on the other hand, there is a large percentage difference between the scattering cross-sections at nonabsorbing wavenumbers greater than 3600 cm^{-1}, decreasing, for example, at 4410 cm^{-1} from 0.122 μm^2 for $\phi = 1$ to 0.094 μm^2 for $\phi = 5$ and 0.076 μm^2 for $\phi = 9$ (an almost 40% reduction compared to $\phi = 1$). This trend is in full accordance with the findings from Zakharova and Mishchenko,[1] demonstrating the reduced scattering efficiencies for needle- and platelike particles in comparison with moderately aspherical particle habits. But as there is only a minor scattering contribution to the overall extinction spectra for 1.0 μm sized ice crystals, these shape-related variations of the scattering cross-sections just have a marginal effect on the general spectral habitus of the midinfrared extinction spectra.

The spectral differences between the various particle shapes become more apparent when the particle size and thus the contribution of scattering to extinction increases.[26] As for the shape-induced variations in the extinction spectra of the 3.1, 5.05, and 7.0 μm sized ice cylinders, we are able to discriminate between two different trends. First of all, in spectral regimes

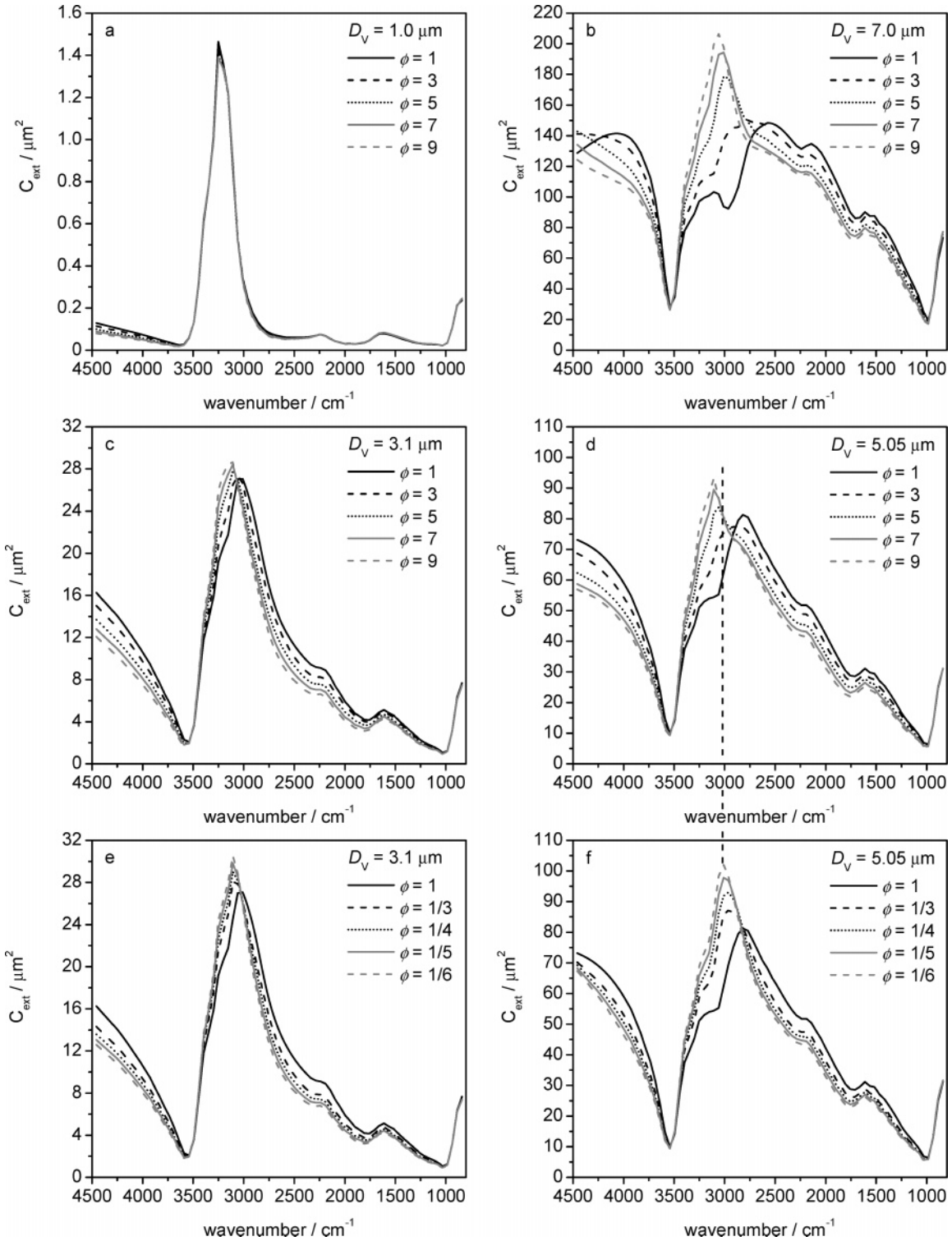

Figure 8. Computed midinfrared extinction cross-sections C_{ext} of cylindrical ice crystals as a function of the aspect ratio ϕ for four discrete ice particle sizes. The individual panels are arranged in such a way to directly compare the results for oblate and prolate particle habits in the cases of the 3.1 and 5.05 μm sized ice crystals.

where the contribution from light absorption is low (2800−1000 cm^{-1}) or completely negligible (4500−3600 cm^{-1}), there is a continuous decrease in the extinction cross-sections with increasing particle asphericity, just reflecting again the reduced scattering cross-sections of highly aspherical ice crystals. But there is one spectral range where the opposite trend is discernible. At wavenumbers between 3500 and 2800 cm^{-1}, comprising the intense O−H absorption band centered at 3250 cm^{-1}, the extinction cross-sections are increasing with an increasing degree of asphericity. The percentage difference between the C_{ext} values for $\phi = 1$ and $\phi = 9$ also increases with increasing ice particle size. For example, at wavenumbers between 3200 and 3000 cm^{-1} and a particle size of $D_V = 7.0$ μm, the extinction cross-sections for platelike $\phi = 9$ ice crystals are enhanced by a factor of 2 compared to compactly shaped $\phi = 1$ cylinders. Exactly the combination of these two contrary effects gives rise to the strong distortion of the spectral habitus of the extinction spectra of highly aspherical ice particles compared to moderately aspherical crystal shapes. As a result of the increasing intensity in the 3500−2800 cm^{-1} regime for strongly aspherical habits,

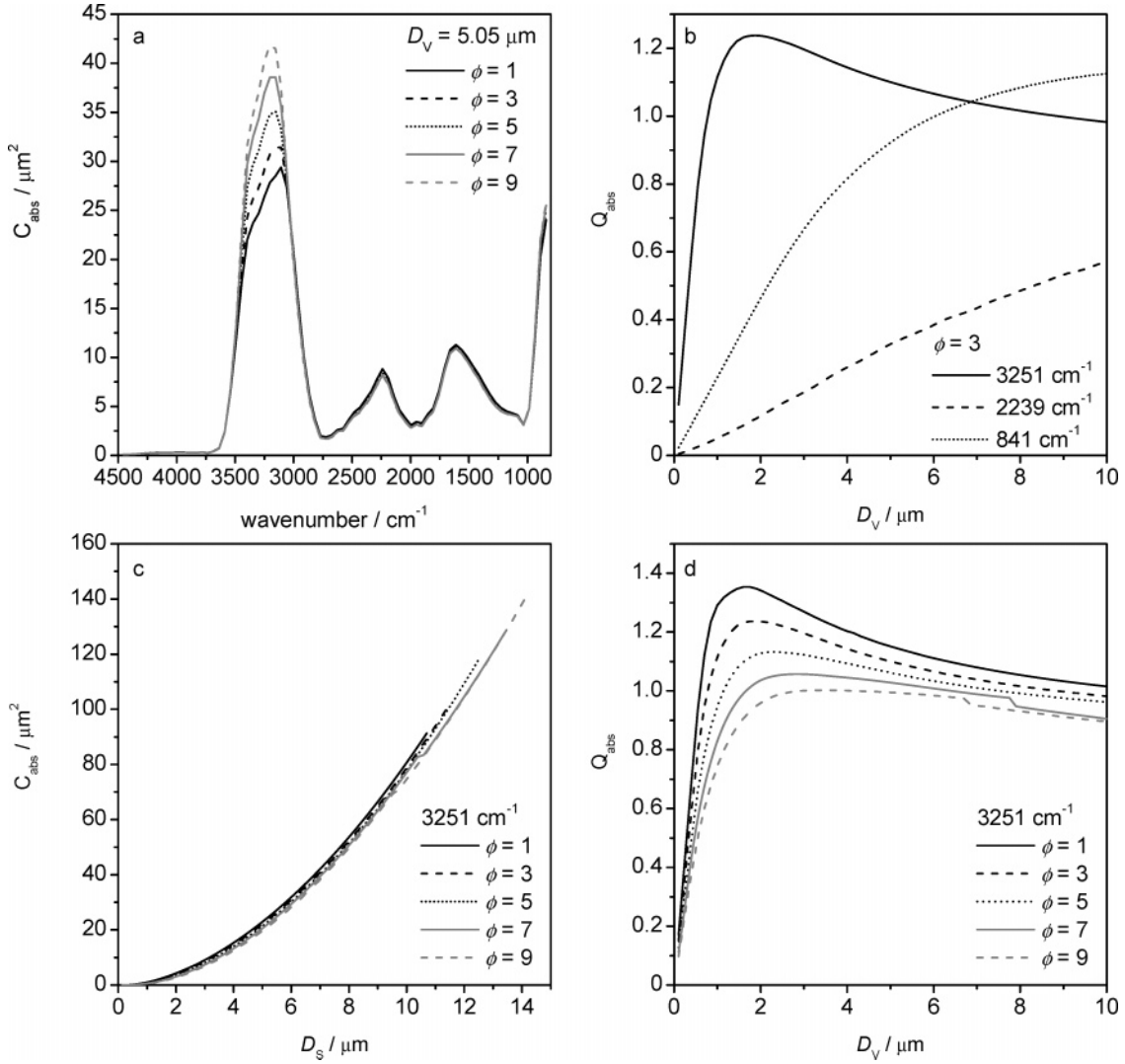

Figure 9. (a) Midinfrared absorption cross-sections of cylindrical ice crystals as a function of the aspect ratio for a fixed particle size of 5.05 μm. (b) Absorption efficiencies for $\phi = 3$ ice cylinders as a function of the equal-volume sphere diameter at three selected wavenumbers. (c) Absorption cross-sections at 3251 cm^{-1} as a function of the equal-surface sphere diameter D_S for variously shaped ice cylinders. (d) Absorption efficiencies at 3251 cm^{-1} as a function of the equal-volume sphere diameter D_V for ice cylinders of different aspect ratios. Note that the small steps occurring in the otherwise smooth Q_{abs} curves for $\phi = 7$ and 9 at $D_V = 7.75$ and 6.7 μm are due to the change from the T-matrix to the DDA code.

the position of the extinction maximum, centered at 3250 cm^{-1} for small ice crystal sizes, does not shift to lower wavenumbers with increasing particle size as characteristic of the $\phi = 1$ crystals (Figure 5). Instead, this effect leads to the spectral trend observed in the spectra series of the expansion runs IN07_22−24; i.e., there is in fact no distinct frequency shift in the position of the extinction maximum as the ice crystals grow in the course of the expansion. As evident from Figure 8, the overall spectral trends are the same for both oblate and prolate particle habits. Nevertheless, as indicated by the vertical dashed line, connecting panels d and f in Figure 8, there are subtle frequency shifts in the position of the extinction maxima for the two different particle geometries that might allow distinguishing between them in the retrieval procedure, as outlined in the final section.

But how can we explain that the spectral range from 3500 to 2800 cm^{-1} reveals such a unique trend in the shape-related variations of C_{ext}, being just opposite to the other wavenumber regimes? To obtain further insight, we will continue our analysis with splitting the overall extinction spectra into their absorption and scattering contributions. Figure 9a shows the shape-induced variations in the midinfrared absorption coefficients C_{abs} for 5.05 μm sized ice cylinders of oblate particle habit. In panel b, we have plotted the size dependence of the absorption efficiencies Q_{abs} (C_{abs} divided through the average cross-sectional areas of the particles, projected on a plane perpendicular to the incident beam) for a fixed particle shape of $\phi = 3$ at three different wavenumbers: 3251, 2239, and 841 cm^{-1}. At these wavenumbers, the bulk absorption coefficient $\alpha(\tilde{\nu}) = 4\pi k(\tilde{\nu})\tilde{\nu}$ for ice varies from $\alpha = 0.1$ μm^{-1} (2239 cm^{-1}) to $\alpha = 0.5$ μm^{-1} (841 cm^{-1}) and $\alpha = 3.27$ μm^{-1} (3251 cm^{-1}). For the weakest absorption band at 2239 cm^{-1}, Q_{abs} almost linearly increases with increasing equal-volume sphere diameter D_V over the considered particle size range. In other words, the absorption cross-sections C_{abs} are proportional to the particle volume and, as shown in panel a, they do not reveal any substantial variation with increasing aspect ratio when D_V is kept constant.

In contrast, for the strong absorption band at 3251 cm^{-1}, the linear relationship between Q_{abs} and D_V only holds for diameters below 1 μm. For larger sizes, Q_{abs} is leveling off, indicating that C_{abs} becomes proportional to the surface area of the particle instead of the particle volume. When plotting the absorption cross-sections at 3251 cm^{-1} as a function of the equal-surface sphere diameter D_S (panel c), the results for all considered particle shapes almost coincide. But as the surface area of ice cylinders with a given equal-volume sphere diameter strongly increases with increasing aspect ratio ϕ, the computed absorption

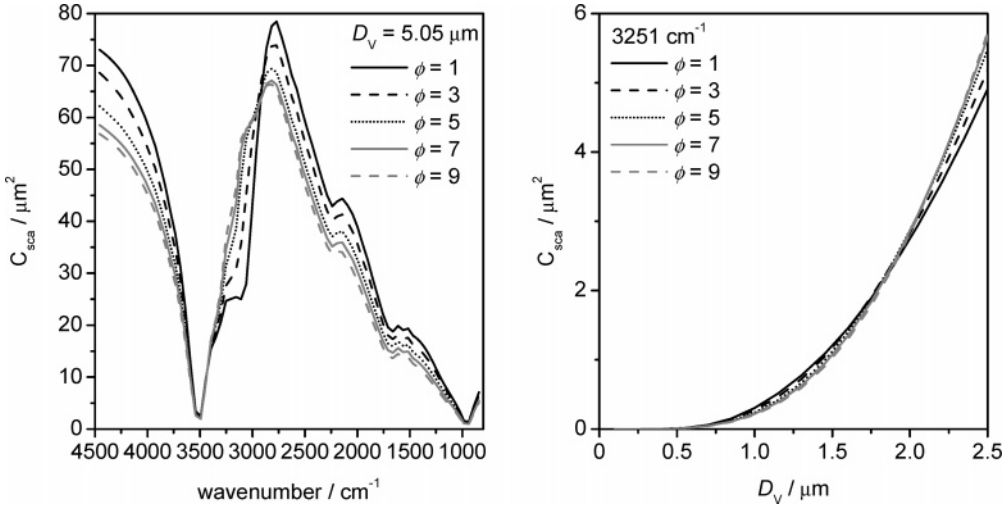

Figure 10. Left panel: Midinfrared scattering cross-sections of cylindrical ice crystals as a function of the aspect ratio for a fixed particle equal-volume sphere diameter of 5.05 μm. Right panel: Scattering cross-sections at 3251 cm^{-1} as a function of the equal-volume sphere diameter D_V for five different ice particle habits.

spectra shown in panel a reveal an increasing intensity at 3251 cm^{-1} for increasing degree of particle asphericity; e.g., C_{abs} for $\phi = 9$ ($D_V = 5.05$ μm) is enhanced by almost 50% compared to $\phi = 1$. At a wavenumber of 841 cm^{-1} with median absorption strength, the $D_V = 5.05$ μm particle size represents the threshold where the linear relationship between Q_{abs} and D_V begins to break down: It just becomes perceptible that the absorption cross-sections slightly increase for the higher aspect ratios.

As a final point we want to note that the C_{abs} versus D_S curves in panel c do not completely overlap. For a given D_S, the absorption cross-sections slightly decrease with increasing particle asphericity. This trend may be explained by a reduction of the absorption resonance for the strongly aspherical particle habits.[27] In panel d, the size dependence of the absorption efficiencies at 3251 cm^{-1} is shown as function of the aspect ratio ϕ. For the most compact ice cylinder with $\phi = 1$, Q_{abs} peaks at a value of 1.35 for $D_V = 1.75$ μm before leveling off toward larger particle sizes. In contrast, for highly aspherical particles with $\phi = 9$, the distinct absorption resonance peak almost disappears. Thus, in the resonance region, the absorption cross-sections at 3251 cm^{-1} are not exclusively a function of the equal-surface sphere diameter of the particles but also depend on their shape. But note that this effect of the reduced absorption efficiencies of, for example, $D_V = 5.05$ μm sized ice crystals with $\phi = 9$ in comparison with compactly shaped $\phi = 1$ cylinders at 3251 cm^{-1} is overcompensated by the higher cross-sectional area of the more aspherical particles; the absorption cross-sections increase with increasing degree of particle asphericity in the regime of the intense O−H absorption band between 3500−2800 cm^{-1}; see panel a. This effect partly accounts for the increased extinction cross-sections of the strongly aspherical ice crystals in just this wavenumber region; but at a closer look it cannot explain this behavior quantitatively. For example, the absolute increase of the extinction cross-section of $D_V = 5.05$ μm sized ice cylinders between $\phi = 9$ and $\phi = 1$ at 3155 cm^{-1} is about 34 μm^2 (Figure 8d). The absolute increase of the absorption cross-section, however, is only about 13 μm^2 (Figure 9a). As a consequence, also the scattering cross-sections C_{sca} of the highly aspherical ice crystals must be enhanced in this particular wavenumber region. This is demonstrated by Figure 10 (left panel), which, analogous to Figure 9a, depicts C_{sca} for variously shaped ice cylinders with $D_V = 5.05$ μm. Obviously, the "normal" trend of diminishing scattering cross-sections for increasing aspect ratios is just inverted in the 3500−2800 cm^{-1} regime.

This behavior might be partially explained as follows: The right panel of Figure 10 shows the shape-dependent scattering cross-sections at 3251 cm^{-1} as a function of D_V. At this strongly absorbing wavenumber, only for small particle sizes with $D_V < 2$ μm the scattering cross-section still decreases with increasing aspect ratio. Above this threshold size, the shape-dependent trend is just inverted; C_{sca} now increases with increasing aspect ratio. Note that for $D_V > 2$ μm all refracted light will be absorbed by the ice particles due to the high imaginary index k at this wavenumber. Consequently, light scattering will now be entirely caused by reflection and diffraction. One might thus conclude that the higher cross-sectional area of the more aspherical ice crystal habits (with identical D_V) leads to a higher diffraction and overall scattering cross-section in the case of opaque ice crystals. But there is another effect that also contributes to the increased scattering cross-sections in the 3500−2800 cm^{-1} regime for strongly aspherical particle habits.

As a basis for discussion, we first introduce another graphical representation for the peculiarity of this wavenumber range concerning shape-related trends in C_{sca}. Figure 11a illustrates that, apart from wavenumbers between 3500 and 2800 cm^{-1}, the midinfrared scattering cross-sections of 5.05 μm sized ice crystals with $\phi = 1$ are perfectly matched by the scattering spectrum of more aspherical ice cylinders with $\phi = 5$ having a slightly larger particle diameter of 5.35 μm. The difference scattering spectrum between the $\phi = 5$ and $\phi = 1$ computations (panel b) is compared to the real and imaginary parts of the complex refractive index of ice (n and k, panels c and d) that were employed in the T-matrix and DDA calculations. ΔC_{sca} peaks at a wavenumber of about 3100 cm^{-1}; this maximum does not coincide with the k absorption maximum at 3250 cm^{-1} but instead with the maximum of the scattering index n in the anomalous dispersion regime. Note that even at a wavenumber of 3000 cm^{-1}, where the value for k is quite low, the scattering cross-section for $\phi = 5$ is clearly higher than that for $\phi = 1$. Therefore, the effect of enhanced diffraction cross-sections at highly absorbing wavenumbers for aspherical particle habits cannot explain the increased scattering cross-sections in the entire 3500−2800 cm^{-1} spectral range. As will be outlined below, also the exceptionally high values for n in this particular

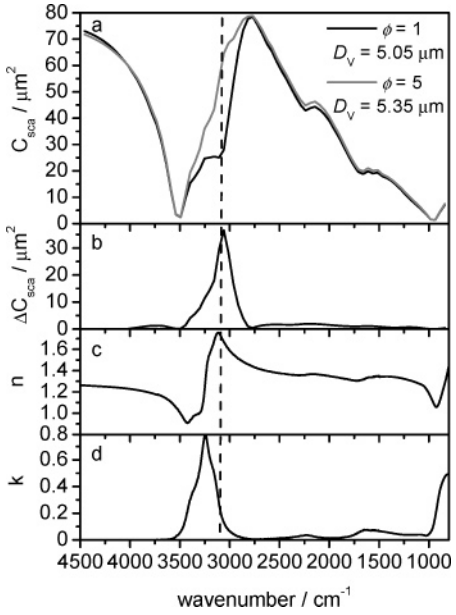

Figure 11. (a) Computed midinfrared scattering cross-sections for two different size/shape combinations of cylindrical ice cylinders. The difference scattering spectrum is shown in panel b. The spectra of the real (panel c) and imaginary (panel d) part of the complex refractive index of ice are shown as a comparison.

wavenumber regime account for the deviations between the two computed spectra shown in panel a.

In Figures 12a and 12b, we show the size-dependent extinction and scattering cross-sections of variously shaped oblate ice cylinders at a wavenumber of 3107 cm^{-1}. Up to an equal-volume sphere diameter of about 2.5 μm, the C_{ext} and C_{sca} curves exhibit the well-known dependence on particle shape, namely, diminishing cross-sections with increasing degree of particle asphericity; see the enlarged frame in panel b. For larger particle sizes, however, the individual traces start to diverge rapidly; for example, for $D_V = 5.05$ μm, the scattering cross-section for $\phi = 9$ ice cylinders is already twice as high as that for compact crystals of $\phi = 1$.

The large divergence of the scattering cross-sections for the various ice crystal shapes at diameters greater than 2.5 μm arises because we enter the size range where the extinction and scattering plots are governed by the characteristic interference structure, i.e., series of extinction maxima and minima caused by interference of incident and forward-scattered light.[28] This can be seen more clearly when plotting the scattering efficiencies as a function of particle size, as done in Figure 12c. We have presented similar plots in our previous work for moderately aspherical ice cylinders; see, for example, top row of Figure 5 therein.[12] For particle sizes larger than the first interference maximum, extinction dramatically varies with particle shape. The regular series of extinction maxima and minima characteristic of spheres is strongly damped and distorted as the degree of particle asphericity increases.[29] In our preceding paper, we have stated that for our considered wavenumber range from 4500 to 800 cm^{-1} the first interference maximum is not reached for ice crystal diameters below about 6 μm. Following the descriptive analysis presented by Bohren and Huffman,[28] the extinction cross-section maxima are approximately determined by the maxima of the function $\sin[x(m-1)]$, which appears in the numerators of the scattering coefficients a_n and b_n, with x denoting the size parameter and m the relative refractive index (ratio of the refractive indices of particle and medium). The first maximum of this function will appear for $(2\pi r/\lambda)(m-1) = \pi/2$ or, solving for the particle radius r, at $r = \lambda/(4(m-1))$. The position of the first interference peak is therefore shifted to larger sizes as the wavenumber and the relative refractive index decrease. For example, for compact ice cylinders and the highest wavenumber of our computations (4456.8 cm^{-1} with $n = 1.26$), the first interference maximum is located at an equal-volume sphere diameter of about 6 μm; for a wavenumber of 1226 cm^{-1} ($n = 1.32$), it is shifted to about 16 μm (Figure 5 in Wagner et al.[12]). But due to the extraordinarily high values for n (up to $n = 1.8$) in the wavenumber region of anomalous dispersion going along with the intense O−H absorption band of ice, the extinction and scattering efficiencies for $\phi = 1$ ice cylinders at 3107 cm^{-1} peak for the first time already at $D_V = 2.5$ μm (Figure 12c). As the imaginary part of the refractive index is not equal to zero at this wavenumber, the interference structure is somewhat dampened, but the first interference maximum is still clearly conserved. For compactly shaped ice crystals, particle sizes greater than about 3.5 μm represent the regime of reduced scattering efficiencies after the first scattering maximum has been surpassed. In contrast, due to the distortion of the interference structure for more aspherical ice crystals, particle sizes in the range $D_V = 5-8$ μm represent the regime of scattering efficiency maxima for oblate ice cylinders with $\phi = 5-10$. For that reason, the scattering cross-sections of 5.05 μm sized ice cylinders (Figure 10) at wavenumbers around 3100 cm^{-1} are enhanced for strongly aspherical particle habits compared to moderately aspherical shapes, thereby contributing to the "unusual" trend in the shape-induced variations of the extinction cross-sections at wavenumbers between 3500 and 2800 cm^{-1}. As a comparison, we have plotted in Figure 12d the scattering cross-section curves for the oblate ice cylinders at a wavenumber of 3975 cm^{-1} with $n = 1.22$. Due to the lower value for n, the common trend of diminishing scattering cross-sections with increasing ϕ is conserved up to a particle diameter of about 7 μm before the strongly shape-dependent interference structure becomes dominant. The onset of divergence of the C_{sca} curves for $D_V > 7$ μm is nicely mapped onto the computed extinction spectra shown in Figure 8b for wavenumbers >4000 cm^{-1}.

The preceding discussion has made clear that the shape-induced variations of the midinfrared extinction spectra of micron-sized aerosol particles in general have to be analyzed for each chemical species on its own. Shape-related trends in the absorption and scattering cross-sections for a given particle size and wavenumber strongly depend on the magnitude of the real and imaginary components of the complex refractive index. Summarizing our results for ice crystals, the main spectral differences between the two computed extinction spectra shown in the bottom left panel of Figure 5 (as well as between the two different measured spectra shown on the right) are due to:

(i) Reduced scattering cross-sections for strongly aspherical $\phi = 5$ ice crystals compared to $\phi = 1$ particles at wavenumber regimes of low absorption between 4500 and 3500 cm^{-1} and between 2800 and 1000 cm^{-1} (because the first interference maximum is not reached at these wavenumbers for this particle size).

(ii) Enhanced absorption cross-sections between 3500 and 2800 cm^{-1} for $\phi = 5$: For the intense O−H absorption band, the absorption cross-sections become sensitive to the surface area of the $D_V = 5.05$ μm sized ice crystals, which is larger for the aspherical particle geometry. This compensates for the slightly lower absorption efficiencies of the $\phi = 5$ ice cylinders. Note that no intensity change is observed for the less intense ice absorption band below 1000 cm^{-1}.

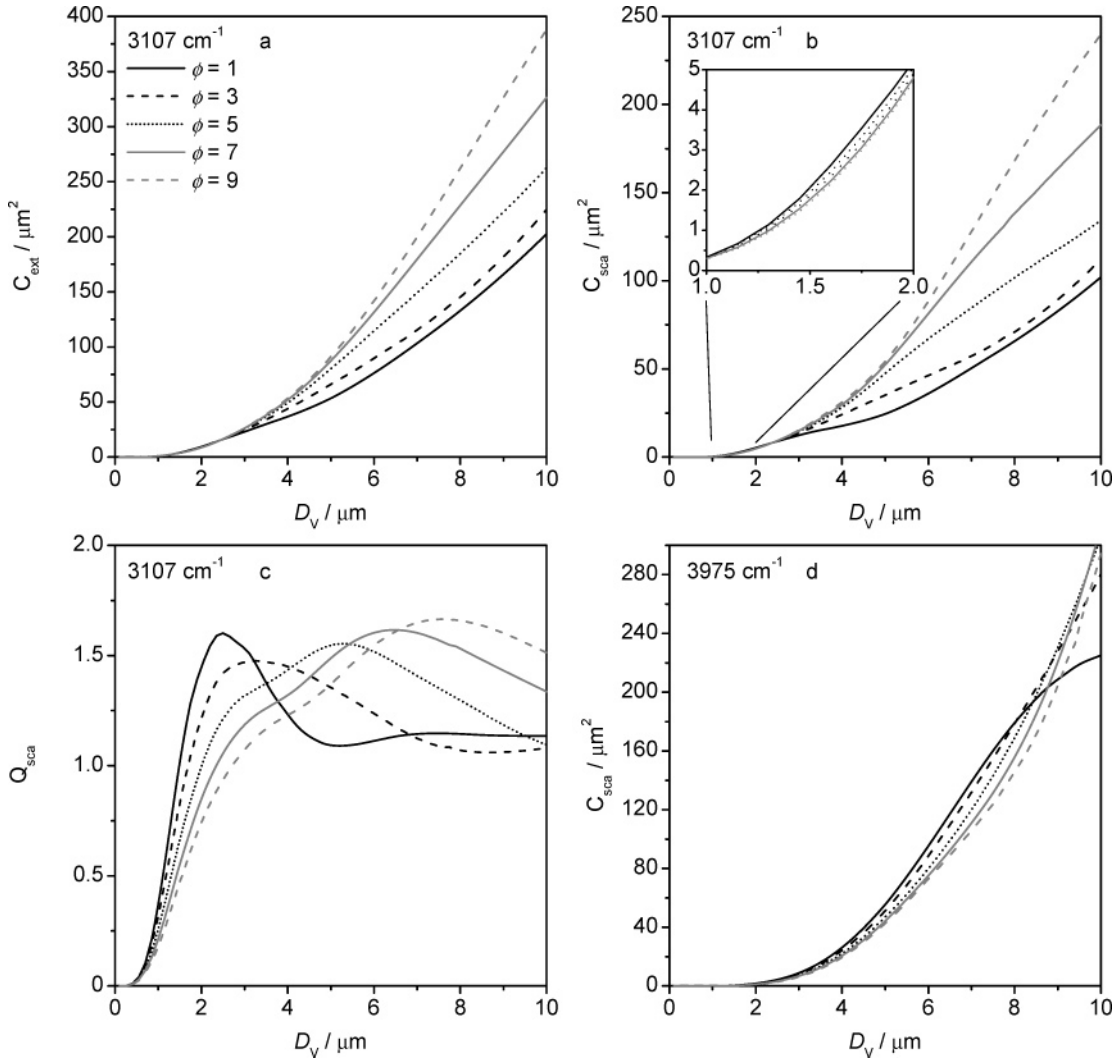

Figure 12. Panels a, b, and c: Extinction cross-sections, scattering cross-sections, and scattering efficiencies at 3107 cm^{-1} as a function of the equal-volume sphere diameter D_V for five different ice particle habits. In panel d, the size-dependent scattering cross-sections are shown for a wavenumber of 3975 cm^{-1}.

(iii) Enhanced scattering cross-sections between 3500 and 2800 cm^{-1} for $\phi = 5$: Due to the high value for n in this wavenumber regime, the first interference maximum for $\phi = 1$ is located at about 2.5 μm (3100 cm^{-1}); for a particle diameter of 5.05 μm, the scattering efficiency has already decreased again. However, for $\phi = 5$, the interference structure is distorted, and $D_V = 5.05$ μm just represents the scattering efficiency maximum. Enhanced diffraction cross-sections at highly absorbing wavenumbers due to the higher cross-sectional area of the $\phi = 5$ ice particles might also partially explain the higher scattering cross-sections in this wavenumber range.

Infrared Retrieval Results for Strongly Aspherical Particle Shapes

In Figures 13 and 14, we have compiled a set of shape-dependent fit results for two selected infrared extinction spectra from the expansion runs IN07_23 and IN07_24, recorded at $t = 447$ s during IN07_23 (Figure 13, same spectrum as in Figure 4) and $t = 407$ s during IN07_24 (Figure 14). Different pure and shape-averaged cylindrical ice particle habits are considered in the retrievals. The ice particle number size distributions, forced to be of the log-normal type, and total number concentrations that best fitted the measured extinction spectra are shown in the top-right corner of each panel. The ice particle number concentrations measured by the OPC at the time of the spectra recordings are $N_{ice} = 12.5 \pm 2.5$ cm^{-3} for IN07_23 and $N_{ice} = 27.5 \pm 5.5$ cm^{-3} for IN07_24. Similar to the fit result from Figure 4 (solid gray line), Figure 13a of Figure 13 underlines that by a strong distortion of the true number size distribution the measured extinction spectrum of highly aspherical ice particles can also be accurately reproduced when considering a compact aspect ratio of $\phi = 1$ in the retrieval. In fact, the $\phi = 1$ fit even results in the smallest spectral residuals of all depicted fit examples. Panel b displays the best fit result for $\phi = 1$ when forcing N_{ice} to be 20 cm^{-3}, i.e., to be close to the OPC reference measurement. The so-derived narrow distribution of larger ice crystals greatly fails to reproduce the measured spectral habitus (Figure 4 (dashed back line)). Thus, an acceptable agreement between both measured and retrieved ice particle number concentration and measured and best fitted extinction spectrum is only obtained for strongly aspherical particle habits.

When assuming that the ice cloud generated during expansion IN07_23 is composed of pure $\phi = 5$, $\phi = 8$, and $\phi = 10$ ice plates (panels c−e), the retrieved N_{ice} data gradually approach the OPC reference value when increasing the aspect ratio; for $\phi = 10$, N_{ice} almost meets the upper error limit of the OPC record. Additionally, in contrast to the $\phi = 1$ fit shown in panel b, a narrow distribution of larger and more aspherical ice crystals

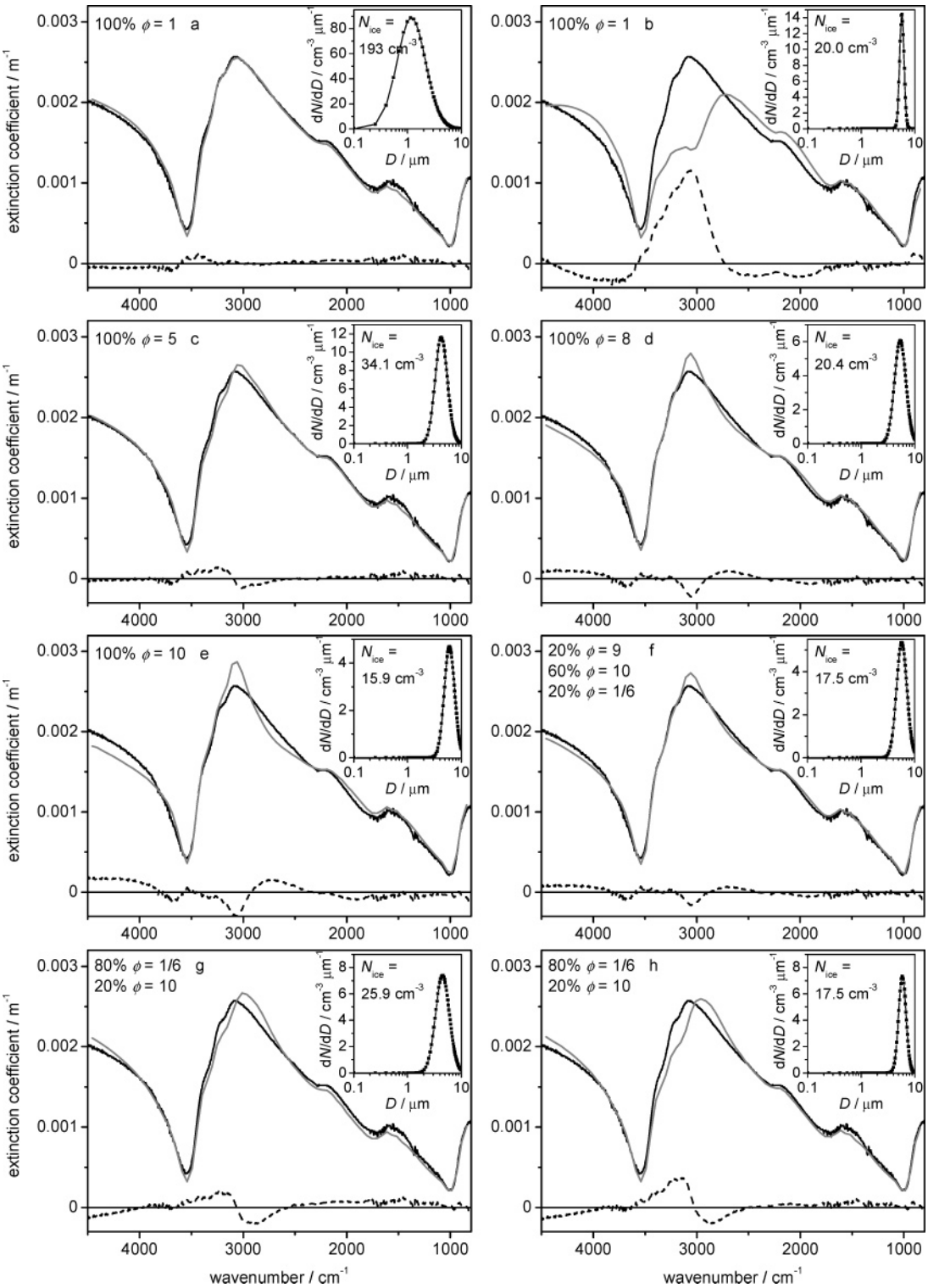

Figure 13. Infrared extinction spectrum of ice crystals recorded at $t = 447$ s during expansion cycle IN07_23 (black line, same as in Figure 4) in comparison with the best fit results for various pure and shape-averaged cylindrical ice particles (gray lines). The spectral residuals (differences from the measured spectrum) are shown as dashed black lines. The retrieved ice crystal number size distributions as well as the ice particle number concentrations (N_{ice}) are displayed in the top-right corner of each panel. For the fits shown in panels a and c−g, N_{ice} as well as the mode widths σ_g and count median diameters D_V were independently optimized; in case studies b and h, N_{ice} was prescribed, and only σ_g and D_V were allowed to vary. $N_{ice} = 12.5 \pm 2.5$ cm^{-3} was measured by the OPC-WELAS.

is able to reproduce the spectral habitus of the measured extinction spectrum fairly well. But, nevertheless, as the agreement between measured and retrieved N_{ice} is getting better, the spectral residuals of the fit results are increasing. Part of the mismatch of, for example, the $\phi = 10$ fit might be due to the fact that our T-matrix and DDA calculations were restricted to an upper particle diameter of 10 μm. The retrieved ice crystal number size distributions suggest that a small number fraction of particles in the actual ice cloud might exceed this threshold size; these particles thus contribute to the measured extinction spectrum but are ignored in the best fitted spectrum. Alternatively, ice particles with even more extreme aspect ratios than those considered in our calculations might have formed. Furthermore, in panel e we have assumed a uniform ice cloud,

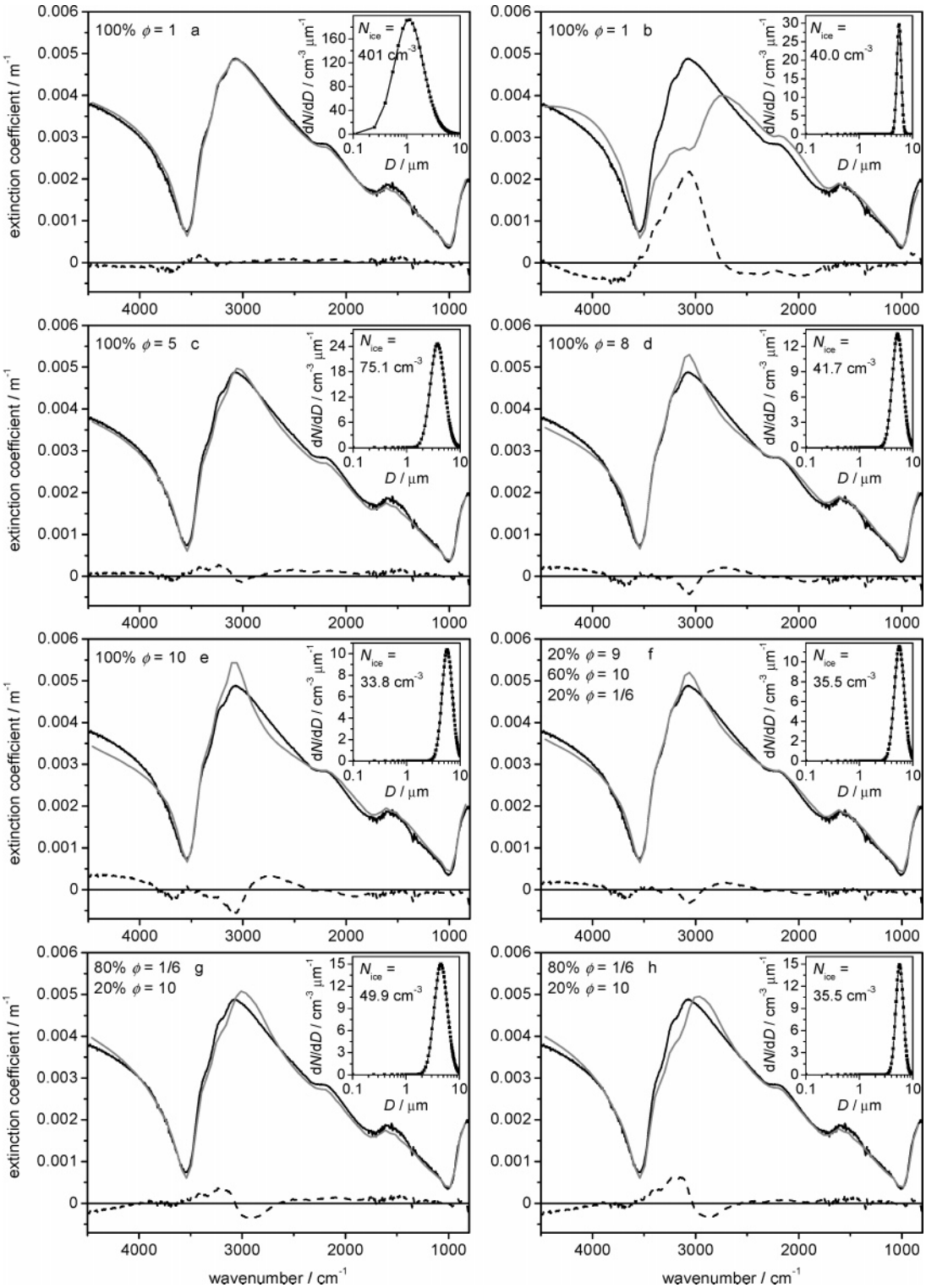

Figure 14. Infrared extinction spectrum of ice crystals recorded at $t = 407$ s during expansion cycle IN07_24 (black line) in comparison with the best fit results for various pure and shape-averaged cylindrical ice particles (gray lines). The spectral residuals (differences from the measured spectrum) are shown as dashed black lines. The retrieved ice crystal number size distributions as well as the ice particle number concentrations (N_{ice}) are displayed in the top-right corner of each panel. For the fits shown in panels a and c−g, N_{ice} as well as the mode widths σ_g and count median diameters D_V were independently optimized; in case studies b and h, N_{ice} was prescribed, and only σ_g and D_V were allowed to vary. $N_{ice} = 27.5 \pm 5.5$ cm^{-3} was measured by the OPC-WELAS.

solely consisting of plates with identical aspect ratios. For the fit shown in panel f, we have employed a shape distribution of cylindrical habits, adding a 20% fraction of columnar ice crystals with $\phi = {}^1/_6$ to an ice cloud otherwise composed of $\phi = 9$ and $\phi = 10$ ice plates. This clearly reduces the spectral residuals compared to the "pure plate" fit scenario, at the same time involving only a slight increase in the retrieved ice particle number concentration, being about 15% above the upper error limit of the OPC reference value. The still remaining spectral mismatch might be caused by: (i) the small percentage deviation between the extinction cross-sections of cylindrical and hexagonal ice crystals, (ii) the approximation in the retrieval procedure that the shape distribution is identical in all individual size bins, (iii) the log-normal constraint on the retrieved size

distribution, and (iv), as stated above, the limitations in the computations with respect to the upper particle diameter and the most extreme aspect ratio. Concerning items ii and iii, we strongly propose to keep the degrees of freedom in the size distribution retrieval for aspherical particles as low as possible. As stated in our previous work, small discrepancies between a measured and a calculated extinction spectrum of an ice cloud, composed of various, partially irregular habits, are virtually unavoidable.[12] Additional degrees of freedom in the retrieval might just lead to an unphysical compensation for the fact that the employed particle shape representation, inevitably, can only be an approximation.

In panel g, we have inverted the shape distribution of fit scenario f, now employing a basically columnar ice crystal habit with $\phi = {}^1/_6$ and including a small contribution of platelike crystals with $\phi = 10$. Thereby, the actual ice particle number concentration is overestimated by a factor of 2. Also, the spectral residuals are larger in comparison with fit example f; in particular, there is a clear 100 cm^{-1} wavenumber shift between the extinction maxima in the measured and computed spectra. When restricting the ice particle number concentration to $N_{ice} = 17.5$ cm^{-3} (panel h), i.e., to be identical to the retrieval result from panel f, the spectral match of the best columnar fit result even gets worse. Although it is difficult to predict how the spectral habitus would evolve for columnar crystals with lower aspect ratios than ${}^1/_6$, this spectral mismatch (see also panels d and f in Figure 8) points to the presence of an ice cloud composed of predominantly platelike ice particle habits.

The preceding discussion, addressing the spectrum recording during experiment IN07_23, holds in the same way for the selected extinction spectrum from activation IN07_24 (Figure 14), illustrating that the generated ice crystal habits must have been very similar in both expansion runs. Once again, the shape distribution with 20% $\phi = 9$, 60% $\phi = 10$, and 20% $\phi = {}^1/_6$ simultaneously provides for a good reproduction of the measured extinction spectrum and an accurate retrieval of N_{ice}. Note that, similar to Figure 13, panels b and h in Figure 14 represent fit results for a fixed ice particle number concentration. In panel b, N_{ice} was constrained to approximate the OPC record (40 cm^{-3}, 20% above the upper error limit of the OPC reference value). For the fit shown in panel h, we again forced N_{ice} to be identical to the retrieval result from panel f.

In Figure 15, we compare the OPC ice particle measurements for the complete time periods of the IN07_23 and IN07_24 expansion runs with the FTIR retrieval results when adopting the shape distribution with 20% $\phi = 9$, 60% $\phi = 10$, and 20% $\phi = {}^1/_6$. For experiment IN07_23, the FTIR retrievals for N_{ice} closely follow the OPC data until $t = 300$ s, exceed the upper error limit of the OPC records by about 15−20% at times between $t = 300$ and 800 s, and again meet the OPC trace at $t > 800$ s. In spite of the small mismatch, this is an immense improvement compared to the large divergence of the FTIR retrievals from the OPC records when employing compact aspect ratios ranging from 0.5 to 3.0; see bottom panel of Figure 4. To account for the remaining discrepancies, the most plausible explanation would be that ice crystals with an aspect ratio slightly higher than $\phi = 10$ have formed during this expansion. The FTIR deduced trace for N_{ice} predicts a maximum at $t = 400$ s, which contradicts the humidity measurements shown in the top panel row of Figure 2. After $t = 300$ s, the saturation ratio with respect to supercooled water starts to drop so that no further ice crystals can nucleate, as confirmed by the OPC measurements, showing an increase in N_{ice} just until $t = 300$ s. But after $t = 300$ s, the chamber air is still supersaturated with respect to ice; the aforegenerated ice crystals will continue to grow due to the uptake of water vapor from the gas phase. Exactly at $t = 400$ s, the maximum of the ice water content of the generated cloud is reached. The degree of asphericity of the ice plates might increase during this time period of ice crystal growth between $t = 300$ and 400 s and might slightly exceed the threshold value of $\phi = 10$, which was employed in our calculations, thereby giving rise to the higher FTIR retrieval results for N_{ice} compared to the OPC data. When the ice crystals start to evaporate at ice subsaturated conditions in the later period of the expansion, the aspect ratio might in turn begin to decrease again, explaining that the FTIR and OPC N_{ice} data converge for $t > 800$ s. For the expansion run IN07_24, these time-dependent trends are only marginally visible; the FTIR retrieval results accurately mimic the $N_{ice}(t)$ trace measured by the OPC over the complete time period of the expansion.

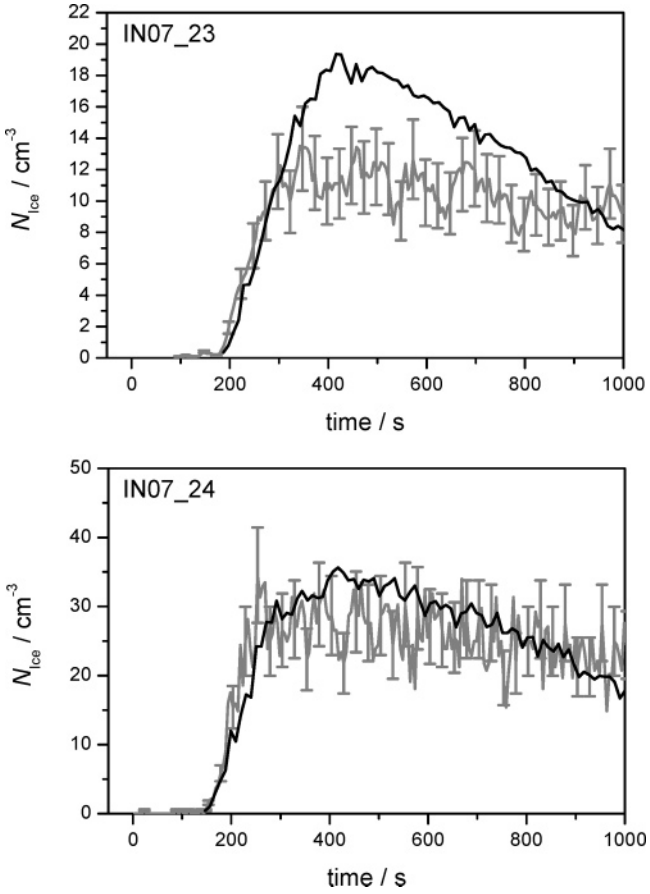

Figure 15. Time series of the ice particle number concentration N_{ice} for expansion experiments IN07_23 and IN07_24 derived from the OPC recordings (gray) and the FTIR extinction measurements (black) when employing a shape distribution of cylindrical ice particles with 20% $\phi = 9$, 60% $\phi = 10$, and 20% $\phi = {}^1/_6$ in the retrieval.

In summary, it is indeed possible to reconcile the infrared retrievals with respect to N_{ice} with the OPC benchmark data for the unusual expansion runs IN07_22−24 when introducing strongly aspherical particle habits. The FTIR analysis points to the presence of predominantly platelike ice crystal habits with an aspect ratio of at least $\phi = 10$. How does this prediction go along with the results from the depolarization measurements? With respect to the quantitative analysis of the depolarization data, the size parameter of the nucleated ice crystals just falls into an intermediate range where it is difficult to find an appropriate theoretical model for solving the scattering problem.[30] The fit results from Figures 13 and 14 suggest that the ice crystals grow to a median equal-volume sphere radius of

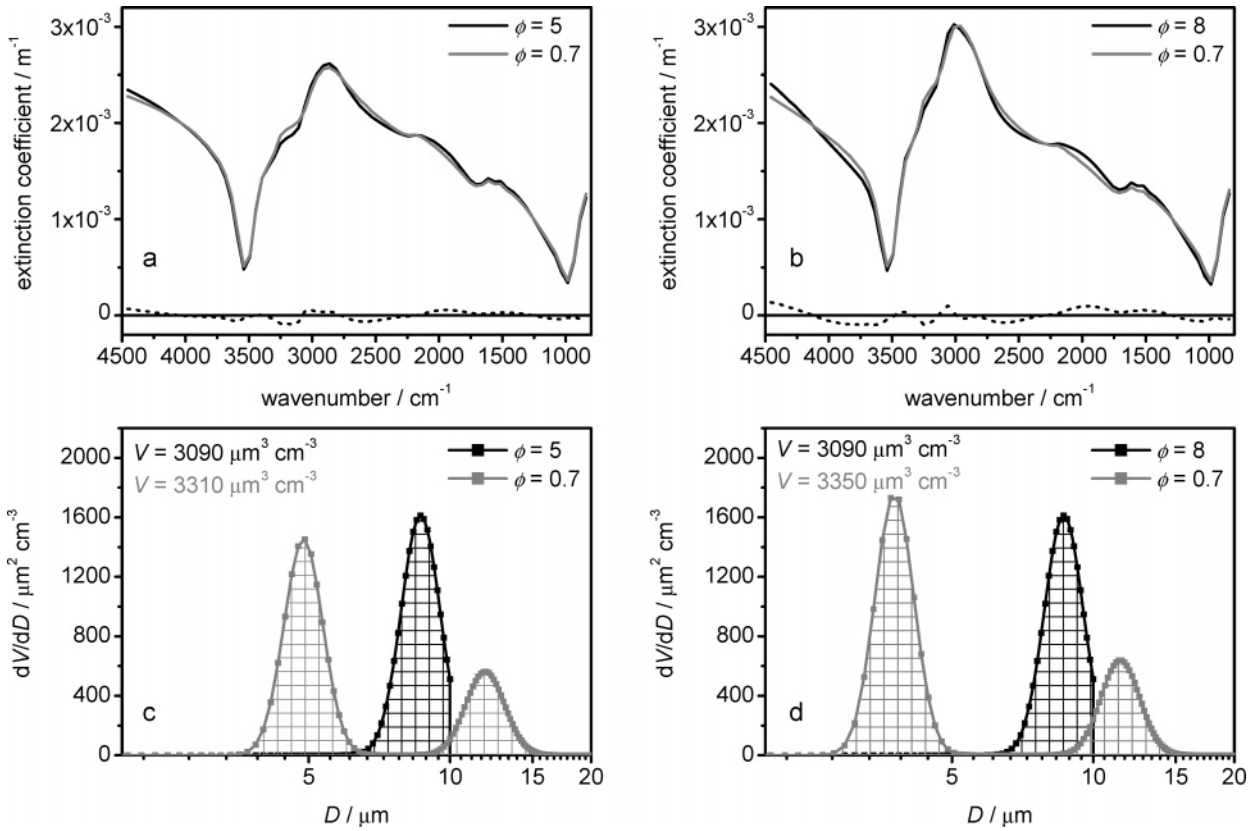

Figure 16. Panels a and b: Calculated infrared extinction spectra of unimodal ice clouds composed of platelike cylindrical ice particles with $\phi = 5$ and $\phi = 8$ for the volume size distributions shown in panels c and d (black lines). Note that these size distributions are truncated at 10 μm, the cutoff size of our T-matrix and DDA calculations for the more extreme aspect ratios. Gray lines indicate the best fitted extinction spectra and deduced volume size distributions when employing a compact aspect ratio of $\phi = 0.7$ and a bimodal size distribution in the retrieval. The total volume concentrations V of ice, obtained by integrating the volume size distributions, are listed in the top-left corner of panels c and d.

about 3 μm during the expansion runs, which is only 6 times larger than the laser wavelength of the depolarization measurements. Hence, the ice crystals will still be too small to consider geometrical optics as a reasonable approximation. However, an equal-volume sphere size parameter x_v of almost 40 (corresponding to an equal-surface sphere diameter x_s of about 56 for $\phi = 10$), in combination with an extreme aspect ratio, will be computationally too demanding or even not solvable for the DDA or T-matrix approach. Please recall that the scattering calculations from Zakharova and Mishchenko[1] for ice spheroids of aspect ratio 20 were restrained to an upper size limit of $x_s = 12$ due to the numerical instability of the T-matrix computations. But the shape-dependent trends in the depolarization ratio δ for such small size parameters might nevertheless give a first indication about the potential degree of asphericity of the larger sized ice crystals from our experiments. In addition, the trace of the depolarization ratio recorded, for example, during expansion IN07_24 reveals that δ already drops to a constant value of 0.04 within the first 50 s after the onset of ice nucleation. At this time, the freshly nucleated ice crystals are still small compared to $t = 400$ s where the maximum of the ice water content of the cloud is reached. In previous test calculations with the T-matrix code,[31] we have computed the depolarization ratio for the scattering geometry of our measurement for oblate ice spheroids with aspect ratios from 2 to 20 in the size range from $x_s = 1$ to 8. As in the Zakharova and Mishchenko[1] study, a narrow gamma distribution of particle sizes with an effective variance of 0.05 was employed. Toward the Rayleigh limit with $x_s = 1$, the depolarization ratio was close to zero for all considered particle shapes. For $\phi = 2$ and $\phi = 5$, the depolarization ratio continuously increased up to $\delta = 0.37$ and $\delta = 0.11$ at $x_s = 8$. This indicates that an aspect ratio of 5 is still not high enough to explain the low depolarization ratio measured during expansions IN07_22−24. Indeed, only for aspect ratios equal to or larger than 10, the depolarization ratio remained at a value smaller than 0.02 also at the highest computed size parameter.

Conclusions

We have demonstrated that the spectral habitus of the infrared extinction spectrum of micron-sized ice crystals undergoes strong distortions when going from moderately to highly aspherical particle habits. The extent of the shape-related spectral changes crucially depends on the magnitudes of the real and imaginary parts of the complex refractive index; it is therefore not possible to simply transfer the present findings to the extinction spectrum of a different chemical species. Unfortunately, regarding the applicability of retrieving accurate number size distributions from the FTIR extinction measurements, the shape-induced distortions of the spectral habitus can also be closely mimicked by deforming the actual size distribution of the ice cloud. Only with the aid of a complementary technique, i.e., the determination of the ice particle number concentration with the WELAS optical particle counter, we could demonstrate that, given the predetermined N_{ice}, highly aspherical ice particle habits are needed to provoke the spectral habitus that was monitored in the expansion experiments IN07_22−24.

Concluding this subject, we want to give another example of the tremendous size/shape ambiguity of the FTIR retrieval results, illustrating that even the modality of the number size distribution of an ice cloud might be falsely predicted. In Figures

16a and 16b, we have computed the infrared extinction spectra of unimodal ice clouds composed of $\phi = 5$ and $\phi = 8$ cylindrical ice plates with a median equal-volume sphere diameter of 8.5 μm (black lines). The corresponding volume size distributions are plotted in panels c and d. The strong spectral distortions, induced by the high value of the aspect ratio, accidentally give rise to a spectral signature that could be fit using a bimodal size distribution when a compact ice crystal shape is employed in the retrieval. Examining, for example, the spectral habitus of the $\phi = 8$ spectrum in panel b with having in mind the signatures characteristic of compact crystal shapes, the pronounced extinction minima (Christiansen bands) at about 3500 and 950 cm^{-1} clearly point to the presence of a fraction of larger ice crystals with $D_V > 10$ μm.[12,32] But, on the other hand, the extinction maximum at 3000 cm^{-1} in combination with the smoothly increasing extinction coefficients between 3700 and 4500 cm^{-1} are typical of smaller, 3−5 μm sized ice crystals. As a result, the extinction spectra of the unimodal ice clouds with $\phi = 5$ and 8 can indeed be accurately fit by a bimodal size distribution of compactly shaped $\phi = 0.7$ particles (gray lines in Figure 16), with one mode of larger and one mode of smaller ice crystals compared to the median size of the unimodal size distribution. In contrast to the different retrievals for the volume size distributions, the overall ice volume concentrations differ by less than 10%.

Focusing on the spectral analysis, we have not addressed so far the question why such highly aspherical ice crystal habits have formed just during the expansion runs IN07_22−24. Arguing that temperature and supersaturation with respect to ice are the key parameters that determine the morphology of the generated ice crystals, it becomes difficult to explain the deviation in the ice particle shape for the experiments IN07_22−24 compared to, for example, experiments IN07_26−28 (pure SOA expansion runs). First of all, the temperature and pressure profile during, for example, the expansion runs IN07_24 and IN07_27 (where the same pumping speed was applied) are virtually identical. Second, also the peak relative humidity with respect to ice coincides for these experiments. There is only a difference in the temporal evolution of S_{ice} after the onset time of ice nucleation (t_{ice}). In experiment IN07_27, the employed seed aerosol number concentration was more than 1 order of magnitude higher than in IN07_24. As a result, more ice crystals have nucleated during IN07_27 (about 150 cm^{-3}, see Figure 3), leading to a rapid depletion of the water vapor and an instant diminishing of the peak ice supersaturation after t_{ice}. In contrast, relative humidity remained close to water saturation for almost 100 s after the onset of ice nucleation for expansion run IN07_24 because the fewer nucleated ice crystals did not deplete the water vapor as efficiently as in experiment IN07_27. One can only speculate that this longer time period of high water vapor supersaturations might be the cause for the formation of the extraordinary ice particle habits. The AIDA expansion runs presented in this study, however, were the first experiments with pure SOA and SOA-coated aerosol particles at a low temperature of 210 K, i.e., using types of aerosol particles that are highly inefficient ice nuclei, thereby leading to such high values for the ice supersaturation in the course of the expansion experiments. It has to be the subject of further chamber studies to investigate whether the formation of the exceptional ice particle habits during IN07_22−24 was just a singular event for a particular type of ice nuclei or can indeed be related to a particular precondition with regard to the prevailing water vapor supersaturation.

Acknowledgment. The authors are grateful for the continuous support by all members of the AIDA staff. We thank U. Schurath for valuable comments on the paper. The work has been funded by the Helmholtz−Gemeinschaft Deutscher Forschungszentren as part of the program "Atmosphere and Climate". Part of this work was also funded within the EU Integrated Project "SCOUT-O3".

References and Notes

(1) Zakharova, N. T.; Mishchenko, M. I. *Appl. Opt.* **2000**, *39*, 5052.

(2) Zakharova, N. T.; Mishchenko, M. I. *J. Quant. Spectrosc. Radiat. Transfer* **2001**, *70*, 465.

(3) Havemann, S.; Baran, A. J. *J. Quant. Spectrosc. Radiat. Transfer* **2004**, *89*, 87.

(4) Pruppacher, H. R.; Klett, J. D. *Microphysics of Clouds and Precipitation*; Kluwer Acacdemic Publishers: Dordrecht, The Netherlands, 1997.

(5) Libbrecht, K. G. *J. Cryst. Growth* **2003**, *258*, 168.

(6) Bailey, M.; Hallett, J. *J. Atmos. Sci.* **2004**, *61*, 514.

(7) Baran, A. J. *J. Quant. Spectrosc. Radiat. Transfer* **2004**, *89*, 17.

(8) Kokhanovsky, A. A. *Earth Sci. Rev.* **2005**, *71*, 127.

(9) Rapp, M.; Thomas, G. E.; Baumgarten, G. *J. Geophys. Res. (Atmos.)* **2007**, *112*, D03211.

(10) Möhler, O.; Field, P. R.; Connolly, P.; Benz, S.; Saathoff, H.; Schnaiter, M.; Wagner, R.; Cotton, R.; Krämer, M.; Mangold, A.; Heymsfield, A. J. *Atmos. Chem. Phys.* **2006**, *6*, 3007.

(11) Wagner, R.; Bunz, H.; Linke, C.; Möhler, O.; Naumann, K. H.; Saathoff, H.; Schnaiter, M.; Schurath, U. Chamber simulations of cloud chemistry: The AIDA chamber. In *Proceedings of the NATO Advances Research Workshop on Environmental Simulation Chambers: Application to Atmospheric Chemical Processes*, Zakopane, Poland, Oct 1−4, 2004, 2006; Springer: Dordrecht, The Netherlands.

(12) Wagner, R.; Benz, S.; Möhler, O.; Saathoff, H.; Schurath, U. *Atmos. Chem. Phys.* **2006**, *6*, 4775.

(13) Ebert, V.; Teichert, H.; Giesemann, C.; Saathoff, H.; Schurath, U. *Tech. Mess.* **2005**, *72*, 23.

(14) Möhler, O.; Stetzer, O.; Schaefers, S.; Linke, C.; Schnaiter, M.; Tiede, R.; Saathoff, H.; Krämer, M.; Mangold, A.; Budz, P.; Zink, P.; Schreiner, J.; Mauersberger, K.; Haag, W.; Kärcher, B.; Schurath, U. *Atmos. Chem. Phys.* **2003**, *3*, 211.

(15) Wagner, R.; Benz, S.; Möhler, O.; Saathoff, H.; Schnaiter, M.; Schurath, U. *J. Phys. Chem. A* **2005**, *109*, 7099.

(16) Benz, S.; Megahed, K.; Möhler, O.; Saathoff, H.; Wagner, R.; Schurath, U. *J. Photochem. Photobiol., A* **2005**, *176*, 208.

(17) Mangold, A.; Wagner, R.; Saathoff, H.; Schurath, U.; Giesemann, C.; Ebert, V.; Krämer, M.; Möhler, O. *Meteorol. Z.* **2005**, *14*, 485.

(18) Murphy, D. M.; Koop, T. *Q. J. R. Meteorol. Soc.* **2005**, *131*, 1539.

(19) Zasetsky, A. Y.; Khalizov, A. F.; Earle, M. E.; Sloan, J. J. *J. Phys. Chem. A* **2005**, *109*, 2760.

(20) Haag, W.; Kärcher, B.; Schaefers, S.; Stetzer, O.; Möhler, O.; Schurath, U.; Krämer, M.; Schiller, C. *Atmos. Chem. Phys.* **2003**, *3*, 195.

(21) Mishchenko, M. I.; Travis, L. D. *J. Quant. Spectrosc. Radiat. Transfer* **1998**, *60*, 309.

(22) Draine, B. T.; Flatau, P. J. *J. Opt. Soc. Am. A* **1994**, *11*, 1491.

(23) Lee, Y. K.; Yang, P.; Mishchenko, M. I.; Baum, B. A.; Hu, Y. X.; Huang, H. L.; Wiscombe, W. J.; Baran, A. J. *Appl. Opt.* **2003**, *42*, 2653.

(24) Rajaram, B.; Glandorf, D. L.; Curtis, D. B.; Tolbert, M. A.; Toon, O. B.; Ockman, N. *Appl. Opt.* **2001**, *40*, 4449.

(25) Clapp, M. L.; Miller, R. E.; Worsnop, D. R. *J. Phys. Chem.* **1995**, *99*, 6317.

(26) Zasetsky, A. Y.; Earle, M. E.; Cosic, B.; Schiwon, R.; Grishin, I. A.; McPhail, R.; Pancescu, R. G.; Najera, J.; Khalizov, A. F.; Cook, K. B.; Sloan, J. J. *J. Quant. Spectrosc. Radiat. Transfer* **2007**, *107*, 294.

(27) Baran, A. J.; Francis, P. N.; Havemann, S.; Yang, P. *J. Quant. Spectrosc. Radiat. Transfer* **2001**, *70*, 505.

(28) Bohren, C. F.; Huffman, D. R. *Absorption and Scattering of Light by Small Particles*; John Wiley & Sons: New York, 1983.

(29) Kocifaj, M.; Horvath, H. *Atmos. Environ.* **2005**, *39*, 1481.

(30) Liu, L.; Mishchenko, M. I. *J. Quant. Spectrosc. Radiat. Transfer* **2001**, *70*, 817.

(31) Büttner, S. Light scattering experiments with aspherical aerosol particles: Depolarisation and forward scattering ratio of mineral dust and ice crystals. Ph.D. Thesis, Institute of Meteorology and Climate Research, Forschungszentrum Karlsruhe, 2004.

(32) Arnott, W. P.; Dong, Y. Y.; Hallett, J. *Appl. Opt.* **1995**, *34*, 541.